Rupture directivity, stress drop, and hypocenter migration of small earthquakes in the Yamagata-Fukushima border swarm triggered by upward pore-pressure migration after the 2011 Tohoku-Oki earthquake

著者	Keisuke Yoshida, Tatsuhiko Saito, Kentaro Emoto, Yumi Urata, Daisuke Sato
journal or publication title	Tectonophysics
volume	769
page range	228184
year	2019-10-20
URL	http://hdl.handle.net/10097/00133202

doi: 10.1016/j.tecto.2019.228184

Rupture directivity, stress drop, and hypocenter migration of small- and moderate-sized earthquakes in the Yamagata-Fukushima border swarm triggered by upward pore-pressure migration after the 2011 Tohoku-Oki earthquake

Keisuke Yoshida[1], Tatsuhiko Saito[2], Kentaro Emoto[1], Yumi Urata[2], Daisuke Sato[3]

1: Department of Geophysics, Graduate School of Science, Tohoku University

2: National Research Institute for Earth Science and Disaster Resilience

3: Research Center for Earthquake Prediction, Disaster Prevention Research Institute, Kyoto University

Corresponding author: Keisuke Yoshida, Research Center for Prediction of Earthquakes and Volcanic Eruptions, Tohoku University, 6-6 Aza-Aoba, Aramaki, Aoba-ku, Sendai, 980-8578, Japan. (keisuke.yoshida.d7@tohoku.ac.jp)

Abstract

We examined a relationship between rupture propagation directions and the distribution of fault strength by analyzing seismological data from the earthquake swarm on the Yamagata-Fukushima border, NE Japan. This earthquake swarm exhibits a distinct hypocenter migration behavior and was estimated to be triggered by upward fluid movement after the 2011 Tohoku-Oki earthquake. We utilized the dense nationwide seismic network in Japan to estimate apparent source time functions of >1,500 small earthquakes ($M_{\mathrm{JMA}} \geq 2$). We found clear directional dependences of the peak amplitude and the pulse-width in the apparent source time functions, suggesting the earthquake rupture directivity, for half of the earthquakes. Based on the unilateral rupture model, rupture directions mostly avoid the directions of the hypocenter migration. The difference between the microscopic and macroscopic propagations of rupture might be explained by the spatial variation in the fault strength affected by pore pressure; ruptures of each earthquake are hindered from developing toward the region with higher fault strength ahead of the pore-pressure front. Estimates of stress drop systematically increased on taking the effects of rupture directivity into account. We observed a temporal increase in stress drop from 3 MPa to 10 MPa during the pore-pressure migration.

1. Introduction

Dynamics of earthquakes and seismicity are dominantly affected by the states of stress and strength on the fault (Das & Aki, 1977; Kanamori & Stewart, 1978). For an improved physical understanding of an earthquake, it is important to examine seismicity and source process on the basis of the spatiotemporal variation in stress and strength. This task is usually challenging because of the lack of information about both stress and frictional states on the fault.

Source process of earthquake, including the initiation, propagation and arrest of rupture, is affected by the spatial distribution of stress and strength on fault (Das & Aki, 1977; Kanamori & Steward, 1978; Madariaga, 1979; Fukuyama & Madariaga, 2000; Urata et al., 2017). In this context, we can consider a basic cause for the rupture directivity: stress and/or strength gradients favoring the rupture of earthquakes toward the direction of reaching the failure criterion (away from areas of low stress or high fault strength). Variation of elastic properties across the fault lead to persistent rupture directivity by the strong dynamic reduction in normal stress (Weertman, 1980; Ben-Zion & Andrews, 1998; Ben-Zion & Huang, 2002; Ampuero & Ben-Zion, 2008). Small-scale heterogeneities in stress, strength, material properties, and/or their transient changes during the propagation might produce essentially random rupture directivities.

Rupture processes of large earthquakes have been widely examined by seismic waveform analysis (Hartzell & Heaton, 1983; Fukuyama and Irikura, 1986) under certain kinematic constraints. Previous studies have investigated their similarities and differences based on seismic waveform inversion under different tectonic regimes (Ye et al., 2016). Since investigations of earthquake rupture processes are usually limited to large earthquakes (M >5–7), it is difficult to discuss the cause of their similarities and differences by comparing many events under the same setting.

Small- and moderate-sized earthquakes (M <~4) are often approximated as point sources. This is because of the difficulty of modeling high-frequency waveforms (> a few Hz) and the lack of signal recorded at the necessary high frequencies due to low sampling rate or noise. As a consequence, the fault plane is indistinguishable between the two nodal planes of a focal mechanism.

Even a small earthquake has a finite fault length and width. Dominant frequency or pulse-width of waveform is often used for the estimation of fault size based on simple symmetrical circular fault models (Brune, 1970; Sato & Hirasawa, 1973; Madariaga, 1976). If the real source process is asymmetrical or exhibits a significant directivity effect, the assumption of isotropic rupture evolution can lead to a large estimation error in the fault size and thus, the stress drops (Kaneko & Shearer, 2015). Recently, as data quantity and quality have improved, directivity effects on seismic waves have been observed for moderate-sized (Hatch et al., 2018; Abercrombie et al., 2017; Boatwright, 2007; McGuire, 2004; Seekins & Boatwright, 2010; Tan & Helmberger, 2010) and even smaller earthquakes (Chen, Jordan, & Zhao, 2010; Folesky et al., 2016; Tomic et al., 2009; Yamada et al., 2005). We can obtain information about the rupture propagation and the fault orientation by analyzing the directional dependence of the seismic wave.

Since an individual earthquake is caused by an increase in stress and/or a reduction in strength, seismicity also should be affected by the evolution of stress and strength in the focal area. Migration of seismicity, which is frequently seen in earthquake swarms, is often interpreted as being associated with pore-pressure diffusion (Shapiro et al., 1997) in the crust. In fact, the migration behavior of hypocenters is similar to that observed in fluid-injection-induced seismicity (Julian et al., 2010; Parotidis et al., 2005). Migration behaviors of hypocenters could provide a clue to spatiotemporal variation in pore pressure and strength on the fault.

The present study estimates the rupture directivity of small earthquakes in the evolving swarm activity in the Yamagata-Fukushima border. This earthquake swarm exhibits a distinct migration behavior of hypocenters and was estimated to be triggered by upward fluid movement after the 2011 Tohoku-Oki earthquake (Yoshida & Hasegawa, 2018b). An important question is how the spatially varying fault strength and pore pressure affect the rupture of individual earthquakes and the evolution of the seismicity. Examining this earthquake swarm provides a unique opportunity for the relationship between the rupture propagation and the distribution of strength and pore pressure on the fault. Since the migration behavior of hypocenters along the planes can be seen as a macroscopic directivity of failure, comparing them with the directions of rupture propagation of individual earthquakes is of interest.

First, we briefly summarize the Yamagata-Fukushima border swarm (Section 2). Then, we describe the methods for determining focal mechanisms, apparent moment rate functions, and rupture parameters (Section 3). The results indicate that half of $M_{\mathrm{JMA}} \geq 2$ earthquakes in the swarm have significant unilateral rupture directivities. Then, we compare directions of rupture propagation and hypocenter migration (Section 4). We also estimate stress drop of earthquakes by taking the effect of rupture directivity into account. We show that stress drops are systematically underestimated if neglecting the effects of rupture directivity (Section 5). Finally, integrating the results of the analyses, we give a comprehensive picture of dynamics of earthquakes and seismicity in the Yamagata-Fukushima swarm (Section 6).

2. The Yamagata-Fukushima border swarm

Several earthquake swarms were initiated in central Tohoku with a delay of days to weeks after the 2011 Tohoku-Oki earthquake, although the earthquake reduced the shear stress magnitude by its static stress change (Yoshida et al., 2012 and 2018). The most intense earthquake swarm is that on the Yamagata-Fukushima border (Figs. 1 and 2); the magnitude of the largest event is M 4.6. More than 14,000 earthquakes with M >1 were detected and listed in the JMA (Japan Meteorological Agency) unified catalog.

Earthquake hypocenters in the Yamagata-Fukushima border swarm were precisely determined by Yoshida & Hasegawa (2018b) based on the double-difference hypocenter relocation method (Waldhauser & Ellsworth, 2000) by using numerous differential arrival time data obtained by waveform cross-correlation (Fig. S1). Also, focal mechanisms of M >1.2 earthquakes were determined by Yoshida et al. (2016) based on the short-period waveforms of P-waves. The relocated hypocenters are concentrated along several sharply defined planes consistent with WNW-ESE compressional reverse-fault focal mechanisms of individual earthquakes. This suggests that individual small- and moderate-sized earthquakes occur on the several macroscopic planar structures.

Previous studies suggested that these earthquake sequences were triggered in response to the increase in pore-pressure due to upwelling fluids specifically due to the reduction in EW compressional stress associated with the Tohoku-Oki earthquake (Terakawa et al., 2013; Okada et al., 2016; Yoshida et al., 2016, 2017, 2018; Yoshida & Hasegawa, 2008a and b). These earthquake sequences are characterized by their swarm-like seismicity pattern with a distinct migration pattern of hypocenters similar to those observed for the fluid-injection induced seismicity (Julian et al., 2010; Rutledge et al., 2004; Shapiro et al., 1997). According to the precise hypocenter relocation, these earthquakes move along several macroscopic planar structures (Yoshida & Hasegawa, 2018a and b). Yoshida & Hasegawa (2018a, b) suggested that crustal fluids started to move after the 2011 Tohoku-Oki earthquake, permeated into several pre-existing planes, reduced the fault strengths, and caused the earthquake sequences and the upward hypocenter migration along the planes.

Previous studies reported temporal changes in focal mechanisms (Yoshida et al., 2016), stress drop, b-values (Yoshida et al., 2017) and background seismicity rate (Yoshida & Hasegawa, 2018b) in accordance with the fault strength (Yoshida et al., 2016). They are consistent with the idea that this swarm was triggered by the temporal change in pore pressure (Fig. 2b–e).

The focal area of the Yamagata-Fukushima border swarm is surrounded by the national dense seismic network (Fig. 1b), which enables us to examine the directional dependence of the waveform.

3. Data and methods

We used waveform data derived from the national routine seismic network deployed around the source region of the swarm (Fig. 1b). The seismic network is composed of seismic stations of Tohoku University, NIED Hi-net, and V-net. They are three-component velocity seismometers with natural frequencies of 1 Hz recorded at a sampling rate of 100 Hz. We attempted to estimate the rupture directivity of 2,271 earthquakes with $M_{\mathrm{JMA}} \geq 2$ for the period from 11 March, 2013 to 19 May, 2013, which were the first 800 days after the 2011 Tohoku-Oki earthquake.

We first determined focal mechanisms of target earthquakes to help constrain the rupture directivity (Subsection 3.1). We then computed apparent source time functions of target earthquakes at each station (Subsection 3.2) and estimated the directions and speeds of ruptures based on the 1-D unilateral rupture model (Haskell, 1964) (Subsection 3.3).

3.1. Estimation of focal mechanisms

Focal mechanisms are helpful to constrain the direction of rupture propagation. We estimated focal mechanisms by using the similarity of waveforms for this work. The method is described in detail in the Appendix.

We used amplitude ratios of P-, SH-, and SV-waves between a target and a reference event. We used 918 earthquakes whose focal mechanisms were determined by Yoshida et al. (2016) for reference events. We computed the moment tensor components of the target earthquake when amplitude ratio data are obtained at more than eight different stations. We estimated uncertainty of focal mechanisms based on 2,000 bootstrap method resamplings. We derived focal mechanisms only when the 90% confidence range of 3-D rotation angle (Kagan, 1991) is less than 30° from the best-solution. As a result, we obtained focal mechanisms for 1,285 earthquakes contributing to the total focal mechanisms number of 2,203 shown in map view in Fig. S2 and in cross-sectional views along the fault strike in Fig. S3. They are characterized by WNW-ESE compressional reverse fault mechanisms consistent with the planar structures of the hypocenters.

3.2. Estimation of apparent source time functions

For deriving information about the rupture directivity of small earthquakes, it is necessary to handle high-frequency waveforms (a few–a few tens Hz). We adopted the EGF (empirical green function) method (Hartzell, 1978) for correcting the site- and path-effects by using nearby earthquakes. We refer to earthquakes for which waveforms are used for EGF as “EGF events”. Transverse components of direct S-waves are used for the estimation of the rupture directivity.

We selected EGF events which satisfy the following criteria: (1) Distance from the target event is <0.5 km according to the relocated catalog. This criterion is stricter than suggested from a systematic study by Kane et al. (2013a). (2) Mean cross-correlation coefficients of band-passed waveform (2–5 Hz) between the target and the EGF event are higher than 0.85 for at least three stations. Similarity of waveform ensures that event locations are sufficiently close and focal mechanisms are similar (Abercrombie et al., 2016). (3) The magnitude of the EGF is at least 0.8 times smaller than the target earthquake.

For waveform deconvolution, we used the iterative time-domain approach developed by Ligorría & Ammon (1999), after Kikuchi & Kanamori (1982). The cut-off frequency of the low-pass (Butterworth-type) filter used in the algorithm was set to be the mean corner frequencies of the source spectra of the target and the EGF earthquakes. We first roughly estimated corner frequency by assuming the stress drop of 1 MPa in accordance with Yoshida et al. (2017) and the source model of Sato & Hirasawa (1973). If the obtained apparent source time function can explain more than 80% of the observed waveforms, we regarded the deconvolution as successful. When there were multiple candidates for EGF earthquakes for a target event, we stored multiple apparent source time functions for the same stations. The rupture directivity was examined only when apparent moment rate functions are obtained at more than eight different stations.

As a result, we obtained 1,596 earthquakes with apparent moment rate functions at more than eight different stations. Four examples of the distribution of apparent moment rate function are shown in Fig. 3. Although shapes of apparent moment rate functions are similar at nearby stations, directional dependencies of amplitudes and widths of apparent moment rate functions are obvious: short pulse-widths and high amplitudes toward one direction, while long pulse-widths and low amplitudes toward the opposite direction. Such a distribution can be easily explained by the unilateral rupture model.

3.3. Estimation of rupture directivity

In order to estimate the rupture directivity, we applied the 1-D unilateral rupture model (Haskell, 1964) to the distribution of apparent moment rate functions obtained in the previous subsection as follows.

$$T_{\mathrm{d}}{}^{uni} = \frac{L}{V_{\mathrm{r}}}\left(1 - \frac{V_{\mathrm{r}}}{V_{\mathrm{S}}}\vec{R}\cdot\vec{U}\right) \tag{2}$$

where $T_{\mathrm{d}}{}^{uni}$ is the apparent rupture duration; L is the fault length; V_{r} and V_{S} are the speeds of rupture and S-wave, respectively; and $\vec{R}$ and $\vec{U}$ represent the unit vector of the rupture propagation and ray direction at the source, respectively.

To avoid the effect of slight differences of the radiation pattern, we did not rely on amplitudes but on pulse-widths of apparent moment rate functions in the estimation of rupture directivity. We used a fit of synthetic triangular pulses to apparent moment rate functions for the measurement of pulse-widths. We applied the same Butterworth low-pass filter as used for the waveform deconvolution to triangular pulses with variable width. By changing the half-widths of the triangular pulses by 0.01 s, we computed the cross-correlation coefficient with the apparent moment rate function and obtained the best-fit pulse-width. We used the mean pulse-width if we had multiple apparent moment rate functions at the same station for an earthquake.

We grid-searched the direction of rupture (measured by azimuth Φ and take-off angle Θ), $\frac{L}{V_\mathrm{r}}$, and $\frac{V_\mathrm{r}}{V_\mathrm{S}}$ which best explain the obtained pulse-widths of apparent moment rate functions based on Eq. (2). Orientations of the rupture directivity were searched on the two nodal planes of focal mechanisms. We changed the rupture duration $\frac{L}{V_\mathrm{r}}$ (0.01–1.00 s) by dividing the interval by 100 grids, the ratio $\frac{V_\mathrm{r}}{V_s}$ (0 – 1.0) between the rupture velocity and the S-wave velocity by dividing the interval by 50 grids, and the direction of the rupture propagation on the plane (0–350°) by dividing the interval by 36 grids. The evaluation function was defined as follows.

$$Var_{\mathrm{uni}} = \sum_{i=1}^{n} \left(T_{\mathrm{d}}{}^{uni}(\Phi_{\mathrm{i}}, \Theta_{\mathrm{i}}) - T_{\mathrm{d}_i} \right)^2 / n \tag{3}$$

where T_{d_i} is the *i*-th observation of pulse-width and n is the number of the observations. We selected one nodal plane with higher Var_{uni} as the fault plane.

The residual of Eq. (3) was compared with that in the case of the uniform pulse width $\overline{T_d}$

$$Var_{\mathrm{mean}} = \sum_{i=1}^{n} \left(\overline{T_d} - T_{\mathrm{d}_i} \right)^2 / n \tag{4}$$

$$VR = 100\left(1 - \frac{Var_{\mathrm{uni}}}{Var_{\mathrm{mean}}}\right) \tag{5}$$

If the rupture is more suitably modeled by a unilateral rupture, VR approaches to 100. Although directional dependencies are clear for all the four earthquakes in Fig. 3, VR for three of four earthquakes are approximately 55 %. We regarded that the rupture has significant unilateral rupture directivity if the reduction of the variance VR in Eq. (5) is higher than 40 %.

We checked the validity of this threshold (VR >40%) based on the Akaike Information Criterion (AIC) (Akaike, 1973; Sakamoto et al., 1986). We assumed that measurement errors of pulse-width follow a Gaussian distribution. The AIC parameter is expressed as $AIC = n \ln 2\pi + n \ln S + n + 2(m+1)$, where S and m are the sum of the squared mean residuals and the number of model parameters, respectively. We assumed $m = 1$ for the uniform pulse-width model and $m = 3$ for the unilateral rupture model. We computed the difference of AICs $\Delta AIC = AIC_{\mathrm{mean}} - AIC_{\mathrm{uni}}$, where AIC_{mean} and AIC_{uni} are AICs of the uniform pulse-width model and the unilateral rupture model, respectively. We regarded the unilateral rupture model to be the better model when ΔAIC is positive. Fig. S4 compares the ratios of positive ΔAIC with VR for 1,596 earthquakes. Above VR >40 %, ΔAIC is positive for almost all the event (>98%).

We estimated the uncertainty range of directivity parameters for each earthquake by applying the above procedure to 2,000 simulated datasets. We assumed that estimation errors of pulse-width follow a Gaussian distribution with standard deviation of the square root of Var_{uni} and produced 2,000 simulated pulse-width datasets. We then determined the 90% confidence interval of the direction of rupture propagation and rupture velocity. Fig. 3 includes examples of estimated orientations and errors of rupture propagation thus determined. We also evaluated the reliability of the fault-plane choice based on the consistency of 2,000 results. We regarded the fault-plane determination as reliable when more than 90% of the choices are consistent with the best solution. Fig. 4 (d) shows the frequency distribution of percentage of choosing the same fault plane as the best solution for 2,000 simulated data. The percentage is higher than 90% for 321 events, for which we could determine the fault planes.

4. Results of rupture directivity

4.1. Significant proportion of unilateral rupture events

By incorporating the effect of unilateral rupture, residuals in pulse-widths decrease more than 40% (i.e., VR >40%) for approximately 50% of target earthquakes (824 of 1,596 event) as shown by the frequency distribution in Fig. 4 (a). This indicates that half of $M_{\mathrm{JMA}} \geq 2$ earthquakes in the swarm have significant unilateral rupture directivities. This observation is similar to recent observations in various regions of the world (e.g., Chen et al., 2003, McGuire, 2004; Yamada et al., 2005; Boatwright, 2007; Seekins & Boatwright, 2010; Lengline & Got, 2011; Kane et al., 2013b; Kurzon et al., 2014; 015; Folesky et al., 2016; Abercrombie et al., 2017). Furthermore, taking the heterogeneities in stress, frictional state, and material properties into account, rupture directivity might be significant for small earthquakes, as considered for large earthquakes (McGuire, 2002; Chounet et al., 2018).

Fig. 4 (e) and (f) show the frequency distributions of $\frac{V_r}{V_s}$ and $\frac{L}{V_r}$, respectively. $\frac{V_r}{V_s}$ and $\frac{L}{V_r}$ are shown only when the confidence intervals are less than 0.3 (668 events) and 0.025 s (648 events), respectively. We determined $\mathrm{M_0}$ by the empirical relationship with the JMA magnitude (Edwards & Rietbrock, 2009) and L by assuming a V_{s} of 3,300 m/s. Rupture duration $\mathrm{T_r} = \frac{L}{V_{\mathrm{r}}}$ shown in Fig. 4 (f) mostly range from 0.05–0.2 s. Positive correlations are recognized between $\mathrm{T_r}$ and L with the seismic moment $\mathrm{M_0}$ (Fig. 5a and b). $\mathrm{M_0}$ increases with the cube of $\mathrm{T_r}$ and L, supporting the scaling relationship of earthquakes (Aki, 1967; Kanamori & Anderson, 1975) and suggesting that V_{r} is almost constant with $\mathrm{M_0}$.

We need to be careful in interpreting the estimated values of $\frac{V_{\mathrm{r}}}{V_{\mathrm{s}}}$ because they are affected by the lack of signal recorded at the necessary high frequencies due to low-pass filter, low sampling rate or noise (Abercrombie et al., 2017). They are as well affected by the assumption of unilateral rupture. We would underestimate the value of $\frac{V_{\mathrm{r}}}{V_{\mathrm{s}}}$ if the real rupture propagates asymmetrically toward all the directions with higher rupture speed. However, obtained $\frac{V_{\mathrm{r}}}{V_{\mathrm{s}}}$ ranges widely from 0.4–1.0 (Fig. 4e) with a mean value of 0.75, which is similar to the typical range of 0.6–0.9 (Geller, 1976; Venkataraman & Kanamori, 2004). We observe a slight increase in $\frac{V_{\mathrm{r}}}{V_{\mathrm{s}}}$ with magnitude from 2.5–3.1 (Fig. 5c). This might reflect the acceleration of the rupture with propagation before reaching the terminal velocity. Furthermore, obtained values of $\frac{V_{\mathrm{r}}}{V_{\mathrm{s}}}$ seems to change with time (Fig. S5) in a similar pattern with fault strength, stress drop, b-value, and background seismicity rate (Fig. 2). We, however, do not go into detail because of the above reasons.

4.2. Comparison between directions of rupture propagation and hypocenter migration

Frequency distributions of obtained azimuths and take-off angles of rupture propagation are shown in Figs. 4 (b) and (c), respectively. The results are used only when the confidence intervals are less than 30° and VR >40% (684 results for azimuth and 427 results for take-off angle). Although they are diverse, we observe that ruptures avoid propagating eastward, or in the direction of hypocenter migration (Fig. 2a), for many earthquakes. Similarly, ruptures tend to proceed downward ($< 90^\circ$ in Fig. 4c) unlike the orientation of the hypocenter migration (Fig. S1).

There are roughly four clusters in the Yamagata-Fukushima border swarm (Fig. 2a). Fig. 6 (a) shows the enlarged views of hypocenter migration in the four clusters. To see the relationship between the orientations of rupture propagation and hypocenter migration in more detail, we separately show the frequency distributions of rupture azimuth in the four clusters in Fig. 7. We can see that the dominant orientations of rupture propagation are different among the clusters. In the western cluster, ruptures tend to propagate to the north. In the northern and southern clusters, ruptures tend to propagate to the south and north. In the central cluster, ruptures tend to propagate to the northwest.

Fig. 7 compares the orientations of hypocenter migration and rupture directivity in the four clusters. We measured the orientations of hypocenter migration for each $M \geq 1$ earthquake by comparing the mean locations of 40 nearby (< 500 m) $M \geq 1$ earthquakes before and after the earthquake. According to the result, ruptures generally do not propagate in the directions of hypocenter migration. In fact, ruptures appear to avoid propagating in the directions of hypocenter migration. This tendency is clearly observed in the western and the northern clusters (Figs. 7a and b), where fault structures are relatively simply. A consistent tendency can be seen for the other two clusters (Figs. 7c and d) as well.

The fault structure is the simplest in the western cluster. We separately plotted rupture propagation directions on the five distinctive macroscopic planes in the western cluster in Fig. 8 along with hypocenters colored by the timing of occurrence. The macroscopic hypocenter migrations proceed to the SE to SSE directions along each plane while ruptures of each earthquake tend to be oriented NNW. Namely, the orientations of the hypocenter migrations, which probably reflect the migration of pore pressure, are opposite to those of rupture propagations of individual earthquakes.

Recent observations of rupture directivity of small and moderate-sized earthquakes suggested the existence of favored orientations of rupture along the same fault (McGuire, 2004; Boatwright, 2007; Seekins & Boatwright, 2010; Lengline & Got, 2011; Kane et al., 2013b; Kurzon et al., 2014; Calderoni et al., 2015). One likely cause of this is the effect of the bimaterial substance across the fault. The effects of bimaterial fault interface might also explain the predominance of unilateral rupture for a global catalog of large earthquakes (McGuire, 2002; Chounet et al., 2018). The diversity in rupture propagation directions obtained in the present study, however, suggests that they are affected by other factors than the bimaterial effect.

Direction of rupture directivity observed in this study tend to avoid the direction of hypocenter migration, probably reflecting the pore-pressure migration. A similar observation was recently obtained for the case of the largest earthquake (M_L~2) in the fluid-injection induced seismicity at Basel, Switzerland (Folesky et al., 2016). We obtained a similar but more robust tendency of the rupture directivity by analyzing more than 1,500 $M_{JMA} > 2$ events from a natural earthquake swarm and by comparing them with the local hypocenter migrations along the planes. Although Folesky et al. (2016) reported that rupture propagation directions depend on magnitude in fluid-injection induced seismicity, we did not recognize a clear relationship of the rupture directivity with size in the present swarm (Fig. 5d). Since they analyzed smaller earthquakes (M_L~1), the results might reflect smaller-scale heterogeneity in stress and/or strength.

The observed tendency may be explained by the distribution of strengths on the fault. Namely, given that the pore pressure diffused from the deeper portion as suggested by the hypocenter migration (Yoshida & Hasegawa, 2018b), pore pressure is higher with increasing depth. Fig. 9 shows a schematic illustration of the rupture of each earthquake and seismicity, that are controlled by the pore pressure distribution. Lower pore pressure and hence higher fault strength tend to hinder the propagation of rupture outward of the pore-pressure front (shallower development) while higher pore pressure tends to allow rupture to propagate inward.

5. Temporal change in stress drop

In Section 4, we reported that even small and moderate-sized earthquakes exhibit significant rupture directivity in the Yamagata-Fukushima border swarm. The predominance of rupture directivity becomes an obstacle when applying the symmetrical circular fault model to earthquakes for estimating geophysical parameters such as source radius, stress drops. Yoshida et al. (2017) estimated a temporal change in stress drop in this region based on the symmetrical circular fault model of Sato & Hirasawa (1973). In this section, we re-examined the temporal variation in stress drop in the Yamagata-Fukushima border swarm by taking the effects of the rupture directivity into account.

5.1. Determination of stress drop based on a general circular fault model

For estimating the stress drop, we approximated earthquake faults by growth of self-similar circular crack similarly to Sato & Hirasawa (1973). We specified the slip inside the crack by employing the static solution of Eshelby (1957) at every instant in time. Instead of assuming ruptures always initiate at the center of the crack as done by Sato & Hirasawa (1973), we allowed ruptures to initiate in an arbitrary point inside the crack based on a special case (circular fault) of the general crack model of Dong & Papageorgiou (2003). In the model, the radius of rupture increases with a constant velocity (V_{r}') while the center of the rupture front moves to the center of the fault. The slip stops when the rupture front reaches the edge of the fault at $t = r/V_{\mathrm{r}}'$. The rupture front propagates with the maximum velocity of $V_{\mathrm{rmax}} = (1 + r')V_{\mathrm{r}}'$ toward the center of the fault while it propagates with the minimum velocity of $(1 - r')V_{\mathrm{r}}'$ toward the opposite direction. Here, r' is the ratio between the distance of the initiation points from the center and the fault radius r.

We computed the apparent moment rate functions by using the analytical solution derived by Dong & Papageorgiou (2003) and measured the pulse-widths for comparing with the observation. We used the same data, same procedure, and same evaluation function (Eq. 5) described in Subsection 3.2 to determine the source parameters. Unlike the 1-D unilateral rupture model, we grid-searched the radius of the circular fault, the maximum rupture velocity, and the initiation point of rupture that best explain observed pulse-widths. We changed the radius of circular fault r (0.01–1.00 km) by dividing the interval by 100 grids, the ratio $\frac{V_{\mathrm{rmax}}}{V_s}$ (0–1.0) between the maximum rupture velocity and the S-wave velocity by dividing the interval by 50 grids, the ratios r' (0.0–1.0) between the distance of the initiation points from the center to the fault radius by dividing the interval by 20 grids, and the direction of the rupture propagation on the plane (0–350°) by dividing the interval by 36 grid.

Radii of circular fault thus determined for 1,596 earthquakes are shown by the frequency distribution in Fig. 10 (a) and by the relationship with magnitude in Fig. 10 (b). Source radii have a positive correlation with magnitude, which is similar to the case of the 1-D unilateral rupture model (Fig. 5b). Rupture initiation points tend to be located in the edge of the fault (r'~1) (Figs. 10 c and d), which supports the validity of the unilateral rupture model in Section 4. We observe a slight increase in $\frac{V_{\mathrm{r}}}{V_{\mathrm{s}}}$ with magnitude (Fig. 10f) as similar to the results of the unilateral rupture model (Fig. 5c).

We computed the stress drop of each earthquake based on the formula of Eshelby (1957):

$$\Delta\sigma = (7/16)(M_0/r^3) \quad (6)$$

where $\Delta\sigma$ is the stress drop.

5.2. Results of stress drop

Fig. 11 (a) shows the frequency distribution of stress drops thus obtained for 1,596 events. The median value is 5.6 MPa, which is a few times larger than that obtained by Yoshida et al. (2017). For comparison, we computed stress drop by fixing $\frac{V_{\mathrm{rmax}}}{V_s} = 0.9$ and r'=0 which corresponds to the model used by Yoshida et al. (2017) and showed the result in Fig. 11 (c). In this case, estimated values of stress drop decrease (Fig. 11i; the median value is 1.9 MPa) and become similar to those by Yoshida et al. (2017). Residuals of pulse-width, however, are significantly high (VR is distributed around 0 %; Fig. 11f) because this model ignores the directional dependency of apparent moment rate function. On the other hand, if we computed stress drop by fixing $\frac{V_{\mathrm{rmax}}}{V_s} = 0.9$ but allowing asymmetrical rupture propagation (r'>0), obtained stress drops (Fig. 11b) and residuals (Fig. 11e) are not very different from those obtained by changing all the parameters (Figs. 11a and d). This indicates that the difference of estimated stress drops by Yoshida et al. (2017) and in this study mainly comes from the incorrect assumption of the symmetrical rupture propagation adopted by Yoshida et al. (2017). These results demonstrate the importance of taking the effects of rupture directivity into account for estimating stress drop.

We compared obtained stress drop with time in Fig. 12 (a). Median stress drops were computed in 25 time-windows having the same number of results. The 95% confidence intervals are estimated based on the standard deviations. Stress drops are small (~ 3 MPa) at the beginning of the swarm activity, and increase with time for ~50 days, after which they become nearly constant (~ 10 MPa). This temporal pattern is consistent with that reported by Yoshida et al. (2017) (Fig. 2c) although the obtained values are systematically higher in the present study. The temporal pattern itself is maintained even in the cases of fixing $\frac{V_{\mathrm{rmax}}}{V_s} = 0.9$ (Fig. 12b) and $\frac{V_{\mathrm{rmax}}}{V_s} = 0.9$ and r'=0 (Fig. 12c).

6. Discussion

6.1. Fault planes of small and earthquakes and macroscopic hypocenter alignments

Rupture directivity is one of the most significant pieces of information about the fault plane of individual earthquake. We examined the relationship between the macroscopic hypocenter alignments and fault planes of individual earthquakes in the Yamagata-Fukushima border swarm directly by employing the rupture directivity.

Orientations of fault planes are separately shown by cross-sectional views in the four clusters in Fig 6 (b). The planar structure of the hypocenter is the clearest in the western cluster, in which most of fault planes dip to the west and parallel to the macroscopic planar structure of the hypocenters. Fault structure is also relatively simple in the northern and central clusters. Fig. 13 shows cross-sectional views of fault planes and hypocenter alignments in the northern to central part of the focal region in more detail along the lines A-P in Fig. 2 (a). Most fault planes are parallel to the west dipping macroscopic planar structures of hypocenters also in this case. This suggests that most of small and moderate-sized earthquakes in the swarm occurred using those common planar structures. This observation is consistent with the hypothesis that this earthquake swarm is caused by the intrusion of fluids from the deeper into several existing planar structures (Yoshida & Hasegawa, 2018b).

By contrast, there are some earthquakes with fault planes perpendicular to the hypocenter alignments. This suggests that there exist branching faults continuing from the dominant faults, and earthquakes also occur along these planes. Some of them might facilitate the upward movement of fluids by connecting the dominant planes. Fault planes in the deeper portion tend to be perpendicular to the macroscopic hypocenter alignments (cross-sections E–H in Fig. 13). They correspond to earthquakes with abnormal fault focal mechanisms reported by Yoshida et al. (2016) in the initial phase (< ~ 50 days after the 2011 Tohoku-Oki earthquake). They suggested that these earthquakes were caused by unfavorably-oriented faults due to the elevated pore pressure. The present observation supports that earthquakes in the initial stage occur on various small-scale fault planes rather than the dominant fault planes.

Fault planes in the southern part of the source region show more complex fault structures in accordance with the hypocenter distribution (Fig. 6b). By taking the limitation of the resolution of hypocenter relocation into account, information from the rupture directivity can be unique data for understanding the fault planes of small and moderate-sized earthquakes.

6.2. Integrated understanding of seismicity and rupture processes in the Yamagata-Fukushima border swarm

The temporal change in stress drop (Fig. 12) is in accordance with those of the fault strength (Fig. 2b), background seismicity rate (Fig. 2d), and b-value (Fig. 2e). Yoshida et al. (2017) and Yoshida & Hasegawa (2018b) suggested that the systematic temporal changes in these parameters together with the upward hypocenter migration can be understood in a consistent manner by the effects of upward fluid diffusion after the 2011

Tohoku-Oki earthquake. Namely, (1) Due to the E-W extension caused by the 2011 Tohoku-Oki earthquake (Yoshida et al., 2012), high-pressure fluid moved from the deeper level and intruded into the source region. (2) The high pore pressure considerably decreased the effective normal stress, decreased the fault strength, and caused intensive seismicity in the region. (3) The reduction in fault strength made earthquake occurrence more likely, even though the stress did not reach high levels, which resulted in a high rate of occurrence of smaller earthquakes. (4) As time elapsed (> 100 days from the Tohoku-Oki earthquake), the fluid diffused over the region, expanding the active swarm area. (5) This expansion decreased the pore pressure, resulting in an increase in the fault strength and the decrease in the earthquake number and b-value around the pore-pressure fronts.

Furthermore, we consider that the characteristics of rupture propagations obtained in this study can be explained by the spatial variation in fault strength due to the pore-pressure migration in a consistent manner with systematic temporal changes in fault strength, stress drop, background seismicity rate, b-values, and upward hypocenter migration. We observed that the orientations of rupture propagation are approximately opposite to those of the hypocenter migration and the pore-pressure migration. This observation is consistent with ruptures of each earthquake being hindered from shallower development due to higher fault strength ahead of the pore-pressure front. Since earthquakes (and possible aseismic slips) already occurred in the deeper portion along the plane, shear stress decreased there. The complex distribution of stress and strength along the fault planes thus produced might have caused some diversity seen in the rupture propagation directions.

The temporal change in stress drop may be explained by considering that it reflects the change in effective normal stress. Yoshida et al. (2017) used the following simplified relationship to explain the obtained correlation between fault strength τ_0 and stress drop $\Delta\sigma$:

$$\tau_0 = \mu_s \sigma_n^{eff} \qquad (6)$$

$$\Delta\sigma = (\mu_s - \mu_d)\sigma_n^{eff} = (1 - \frac{\mu_d}{\mu_s})\tau_0 \qquad (7)$$

where μ_s, μ_d, and σ_n^{eff} are the static frictional coefficient, kinematic frictional coefficient, and effective normal stress, respectively. Previous studies of fluid-injection induced seismicity support the correlation between stress drops and effective normal stress (Goertz-Allmann et al., 2011; Lengliné et al., 2014).

By taking the finite rupture area into account, this simplification might no longer be valid because initial shear stress τ_{ini} should be smaller than $\tau_0 = \mu_s \sigma_n^{eff}$ except for at the hypocenter. In this case, we should assume $\Delta\sigma = \tau_{ini} - \mu_d \sigma_n^{eff}$ in the surrounding area. This equation implies a negative correlation between stress drop and effective normal stress.

As an alternative method, we might explain the positive relationship between stress drop and fault strength by considering the small-scale stochastic heterogeneity in shear stress (τ_{ini}) in the focal region. Earthquakes can occur even under relatively low magnitudes of shear stress when pore-pressure level is high and effective normal stress is low. By contrast, earthquakes can only occur in higher shear stress region when the pore-pressure level is lower. This suggests that the mean value of shear stress increased during the pore-pressure diffusion, which might have produced the obtained positive relationship between stress drop and fault strength. In fact, Yoshida et al. (2016) suggested that earthquakes occurred on unfavorably-oriented faults, on which shear-stress magnitude is low, especially in the initial stage of this swarm activity.

7. Conclusion

In this study, we investigated the rupture directivities of small and moderate-sized earthquakes in the Yamagata-Fukushima border earthquake swarm, which was estimated to be triggered by upward fluid movement after the 2011 Tohoku-Oki earthquake. We utilized the dense nationwide seismic network in Japan to estimate the rupture directivity of small- and moderate-size earthquakes ($M_{\mathrm{JMA}} \geq 2$).

Apparent source time functions were computed for 1,596 earthquakes at each station based on the waveform deconvolution technique with nearby (<300 m) small earthquakes to remove the propagation- and site-effects. We found clear directional dependences of the peak amplitude and the pulse-width in the apparent source time functions, suggesting the earthquake rupture directivity, for 824 of 1,596 event.

Based on the unilateral rupture model, we estimated the direction, duration, and velocity of rupture for each earthquake. Rupture directions of most earthquakes tend to be different from those of the hypocenter migration. This difference between the microscopic and macroscopic propagations of rupture might be explained by the spatial variation in the fault strength on the fault; ruptures of each earthquake are hindered in their development toward the region with higher fault strength ahead of the pore-pressure front. This suggests the importance of the knowledge of spatial variation in fault strength affected by pore pressure to understand source processes.

Fault planes of small and moderate-sized earthquakes were estimated based on focal mechanism and rupture directivity. Most of the fault planes are parallel to the macroscopic planar structures, which is consistent with the idea that they were triggered by fluid intrusion along those common planar structures. By taking the limitation of the resolution of hypocenter relocation, information from the rupture directivity can provide unique data for understanding the fault planes of small and moderate-sized earthquakes.

We confirmed the temporal increase in stress drop reported by Yoshida et al. (2017) by taking the effect of rupture directivity into account, although the obtained values are systematically higher in the present study. The systematic temporal changes in fault strength, stress drop, background seismicity rate, b-values, the upward hypocenter migration along the planar structures, and the rupture directivity opposite to the hypocenter migration can be explained in a consistent manner by the effects of the upward fluid flow along several existing planes after the 2011 M9 Tohoku-Oki earthquake.

Appendix

We determined the focal mechanism to obtain information about fault planes of individual earthquakes. For that, we used amplitudes of direct P- and S-wave corrected by those of a reference earthquake whose focal mechanism is known. We adopted a similar method to Dahm (1996), which utilizes amplitude ratios of P-, SH-, and SV-waves by assuming that the medium in the vicinity of the source is homogeneous and isotropic. The displacement component u_i^n in the n direction for phase observation i is:

$$u_i^n = I_i^n \sum_{k=1}^{6} m_k a_{ik} \quad (1)$$

with

P: $a_{i1} = -\sin^2\theta_i \cos 2\varphi_i$, $a_{i2} = -\sin^2\theta_i \sin 2\varphi_i$, $a_{i3} = \sin 2\theta_i \cos\varphi_i$, $a_{i4} = \sin 2\theta_i \sin\varphi_i$, $a_{i5} = \sin^2\theta_i - 2\cos^2\varphi_i$, $a_{i6} = 1$,

SH: $a_{i1} = -\sin\theta_i \sin 2\varphi_i$, $a_{i2} = -\sin\theta_i \cos 2\varphi_i$, $a_{i3} = -\cos\theta_i \sin\varphi_i$, $a_{i4} = \cos\theta_i \sin\varphi_i$, $a_{i5} = 0$, $a_{i6} = 0$,

SV: $a_{i1} = -\frac{1}{2}\sin 2\theta_i \cos 2\varphi_i$, $a_{i2} = \frac{1}{2}\sin 2\theta_i \sin 2\varphi_i$, $a_{i3} = \cos 2\theta_i \cos\varphi_i$, $a_{i4} = \cos 2\theta_i \sin\varphi_i$, $a_{i5} = \frac{3}{2}\sin 2\theta_i$, $a_{i6} = 0$,

and

$m_1 = 0.5(M_{22} - M_{11})$, $m_2 = M_{12}$, $m_3 = M_{13}$, $m_4 = M_{23}$, $m_5 = \frac{1}{3}(0.5(M_{22} + M_{11}) - M_{33})$, $m_6 = \frac{1}{3}(M_{11} + M_{22} + M_{33})$

where M_{lm} are the moment tensor components, and φ_i and θ_i are the azimuth and take-off angle of the ith ray (Dahm, 1996). I_i^n includes the site- and path-effects. We cancel out I_i^n in Eq. (1) by considering amplitude ratios between a target event and a reference event. By substituting the moment tensor components of the reference event, we obtain a set of linear equations that relate the moment tensor components of the target events to amplitude ratio data. To validate the assumption for cancelling out I_i^n and to obtain the amplitude ratios robustly, amplitude ratio data are discarded if the two waveforms are not similar (cross correlation coefficient less than 0.6). We use low-frequency (2–5 Hz) waveforms for avoiding the effect of rupture directivity and measure the amplitude ratio by a principal component fit (Shelly et al., 2013). If amplitude ratio data are obtained at more than eight different seismic stations, we compute the moment tensor components by applying the least square method to the set of linear equations.

Moment tensor components of the reference event were computed under the assumption that they have no non-double-couple components. We limited distance between a target and a reference event to <3 km. We computed 2,000 focal mechanisms for each target event based on bootstrap resampling of amplitude ratio data. Difference of focal mechanisms from the best-solution is measured by the 3-D rotation angle (Kagan, 1991). If the 90 % confidence region was larger than 30°, we discarded the result. Thus, moment tensor solutions of 1,285 $\mathrm{M_{JMA}} \geq 2$ events were determined.

Fig. A1 shows an example of applying this method to an aftershock of the 2008 Iwate-Miyagi Nairiku earthquake. The focal mechanism of this earthquake was precisely determined by Yoshida et al. (2014) based on P-wave first-motion polarity data owing to the temporal seismic network (Fig. A1a). We newly determined the focal mechanism of this earthquake by the above procedure using only the routine seismic network data. The result is almost identical to that obtained by Yoshida et al. (2014).

Acknowledgments

We deeply thank the editor Kelin Wang, Rachel E. Abercrombie, and an anonymous reviewer for their constructive comments, which helped to improve the manuscript. The comments from Roland Bürgmann on the first draft significantly improved the manuscript. KY thanks Hiroo Kanamori for motivating and helping the investigation of rupture directivity of small earthquakes in the first stage. The figures in the present paper were created using GMT (Wessel and Smith, 1998). Focal mechanisms, rupture directivities, and stress drops determined in this study are accessible via the following address: http://www.aob.gp.tohoku.ac.jp/~yoshida/pub/Tecto2019/.

References

Abercrombie, R. E., Bannister, S., Ristau, J., & Doser, D., 2016. Variability of earthquake stress drop in a subduction setting, the Hikurangi Margin, New Zealand. Geophysical Journal International, ggw393.

Abercrombie, R.E., Poli, P., Bannister, S., 2017. Earthquake Directivity, Orientation, and Stress Drop Within the Subducting Plate at the Hikurangi Margin, New Zealand. J. Geophys. Res. Solid Earth 122, 10, 176-10, 188. https://doi.org/10.1002/2017JB014935

Ampuero, J.P., Ben-zion, Y., 2008. Cracks, pulses and macroscopic asymmetry of dynamic rupture on a bimaterial interface with velocity-weakening friction. Geophys. J. Int. 173, 674–692. https://doi.org/10.1111/j.1365-246X.2008.03736.x

Bachmann, C.E., Wiemer, S., Goertz-Allmann, B.P., Woessner, J., 2012. Influence of pore-pressure on the event-size distribution of induced earthquakes. Geophys. Res. Lett. 39, 1–7. https://doi.org/10.1029/2012GL051480

Ben-Zion, Y., Andrews, D.J., 1998. Properties and implications of dynamic rupture along a material interface. Bull. Seismol. Soc. Am , 88(4), 1085-1094.

Ben-Zion, Y., Huang, Y., 2002. Dynamic rupture on an interface between a compliant fault zone layer and a stiffer surrounding solid. J. Geophys. Res. 107, 2042. https://doi.org/10.1029/2001JB000254

Boatwright, J., 2007. The persistence of directivity in small earthquakes. Bull. Seismol. Soc. Am. 97, 1850–1861. https://doi.org/10.1785/0120050228

Brune, J.N., 1970. Tectonic stress and the spectra of seismic shear waves from earthquakes. J. Geophys. Res. 75, 4997–5009. https://doi.org/10.1029/JB075i026p04997

Chen, P., Jordan, T.H., Zhao, L., 2010. Resolving fault plane ambiguity for small earthquakes. Geophys. J. Int. 181, 493–501. https://doi.org/10.1111/j.1365-246X.2010.04515.x

Chounet, A., Vallée, M., Causse, M., Courboulex, F., 2018. Global catalog of earthquake rupture velocities shows anticorrelation between stress drop and rupture velocity. Tectonophysics 733, 148–158. https://doi.org/10.1016/j.tecto.2017.11.005

Dahm, T., 1996. Relative moment tensor inversion based on ray theory: Theory and synthetic tests. Geophys. J. Int. 124, 245–257. https://doi.org/10.1111/j.1365-246X.1996.tb06368.x

Das, S., & Aki, K., 1977, Fault plane with barriers: a versatile earthquake model. Journal of geophysical research, 82(36), 5658-5670.

Dong, G., Papageorgiou, A.S., 2003. On a new class of kinematic models: Symmetrical and asymmetrical circular and elliptical cracks. Phys. Earth Planet. Inter. 137, 129–151. https://doi.org/10.1016/S0031-9201(03)00012-8

Edwards, B., Rietbrock, A., 2009. A comparative study on attenuation and source-scaling relations in the Kantō, Tokai, and Chubu regions of Japan, using data from Hi-net and KiK-net. Bull. Seismol. Soc. Am. 99, 2435–2460. https://doi.org/10.1785/0120080292

Folesky, J., Kummerow, J., Shapiro, S.A., Häring, M., Asanuma, H., 2016. Rupture directivity of fluid-induced microseismic events: Observations from an enhanced geothermal system. J. Geophys. Res. Solid Earth 121, 8034–8047. https://doi.org/10.1002/2016JB013078

Fukuyama, E., Irikura, K., 1986. RUPTURE PROCESS OF THE 1983 JAPAN SEA (AKITA-OKI) EARTHQUAKE USING A WAVEFORM INVERSION METHOD. Bull. Seismol. Soc. Amerma 76, 1623–1640. https://doi.org/10.1785/0119990070

Fukuyama, E., Madariaga, R., 2000. Dynamic Propagation and Interaction of a Rupture Front on a Planar Fault. Pure Appl. Geophys. 157, 1959–1979. https://doi.org/10.1007/PL00001070

Geller, R.J., 1976. SCALING RELATIONS FOR EARTHQUAKE SOURCE PARAMETERS AND MAGNITUDES, Bulletin of the Seismological Society of America.

Goertz-Allmann, B.P., Goertz, A., Wiemer, S., 2011. Stress drop variations of induced earthquakes at the Basel geothermal site. Geophys. Res. Lett. 38, n/a-n/a. https://doi.org/10.1029/2011GL047498

Hainzl, S., Ogata, Y., 2005. Detecting fluid signals in seismicity data through statistical earthquake modeling. J. Geophys. Res. Solid Earth 110, 1–10. https://doi.org/10.1029/2004JB003247

Hartzell, B.Y.S.H., Heaton, T.H., 1983. INVERSION OF STRONG GROUND MOTION AND TELESEISMIC WAVEFORM DATA FOR THE FAULT RUPTURE HISTORY OF THE 1979 IMPERIAL VALLEY, CALIFORNIA, EARTHQUAKE. Bull. Seismol. Soc. Am. 73, 1553–1583.

Hartzell, S.H., 1978. Earthquakes aftershocks as Green's Functions. Geophys. Res. Lett. 5, 1–4. https://doi.org/10.1029/GL005i001p00001

Hasegawa, A., Umino, N., Takagi, A., 1978. Double-planed structure of the deep seismic zone in the northeastern Japan arc. Tectonophysics 47, 43–58. https://doi.org/10.1016/0040-1951(78)90150-6

Haskell, N.A., 1964. Total energy and energy spectral density of elastic wave radiation from prom propagating faults. Bull. Seismol. Soc. Am. 54, 1811–1841. https://doi.org/10.1029/SP030p0149

Hatch, R. L., Abercrombie, R. E., Ruhl, C. J., & Smith, K. D., 2018. Earthquake Interaction, Fault Structure, and Source Properties of a Small Sequence in 2017 near Truckee, California. Bulletin of the Seismological Society of America, 108(5A), 2580-2593.

Iinuma, T., Hino, R., Kido, M., Inazu, D., Osada, Y., Ito, Y., Ohzono, M., Tsushima, H., Suzuki, S., Fujimoto, H., Miura, S., 2012. Coseismic slip distribution of the 2011 off the Pacific Coast of Tohoku Earthquake (M9.0) refined by means of seafloor geodetic data. J. Geophys. Res. Solid Earth 117, 1–18. https://doi.org/10.1029/2012JB009186

Julian, B.R., Foulger, G.R., Monastero, F.C., Bjornstad, S., 2010. Imaging hydraulic fractures in a geothermal reservoir. Geophys. Res. Lett. 37. https://doi.org/10.1029/2009GL040933

Kanamori, H., & Stewart, G. S., 1978, Seismological aspects of the Guatemala earthquake of February 4, 1976. Journal of Geophysical Research: Solid Earth, 83(B7), 3427-3434.

Kane, D. L., Kilb, D. L., & Vernon, F. L., 2013a, Selecting empirical Green's functions in regions of fault complexity: A study of data from the San Jacinto fault zone, southern California. Bulletin of the Seismological Society of America, 103(2A), 641-650.

Kane, D.L., Shearer, P.M., Goertz-Allmann, B.P., Vernon, F.L., 2013b. Rupture directivity of small earthquakes at Parkfield. J. Geophys. Res. Solid Earth 118, 212–221. https://doi.org/10.1029/2012JB009675

Kaneko, Y., Shearer, P.M., 2015. Variability of seismic source spectra, estimated stress drop, and radiated energy, derived from cohesive-zone models of symmetrical and asymmetrical circular and elliptical ruptures. J. Geophys. Res. Solid Earth 120, 1053–1079. https://doi.org/10.1002/2014JB011642

Kurzon, I., Vernon, F.L., Ben-Zion, Y., Atkinson, G., 2014. Ground Motion Prediction Equations in the San Jacinto Fault Zone: Significant Effects of Rupture Directivity and Fault Zone Amplification. Pure Appl. Geophys. 171, 3045–3081. https://doi.org/10.1007/s00024-014-0855-2

Lengliné, O., Got, J.L., 2011. Rupture directivity of microearthquake sequences near Parkfield, California. Geophys. Res. Lett. 38, 1–5. https://doi.org/10.1029/2011GL047303

Lengliné, O., Lamourette, L., Vivin, L., Cuenot, N., & Schmittbuhl, J., 2014. Fluid‐induced earthquakes with variable stress drop. Journal of Geophysical Research: Solid Earth, 119(12), 8900-8913.

Ligorría, J.P., Ammon, C.J., 1999. Iterative deconvolution and receiver-function estimation. Bull. Seismol. Soc. Am. 89, 1395–1400. https://doi.org/10.1016/S0304-3940(97)00816-1

Madariaga, R., 1976. Dynamics of an expanding circular fault. Bull. Seismol. Soc. Am. 66, 639–666. https://doi.org/10.1111/j.1461-0248.2009.01352.x

Madariaga, R., 1979. On the relation between seismic moment and stress drop in the presence of stress and strength heterogeneity. Journal of Geophysical Research: Solid Earth, 84(B5), 2243-2250.

Madariaga, R., Ruiz, S., 2016. Earthquake dynamics on circular faults: a review 1970–2015. J. Seismol. 20, 1235–1252. https://doi.org/10.1007/s10950-016-9590-8

Martínez-Garzón, P., Kwiatek, G., Sone, H., Bohnhoff, M., Dresen, G., Hartline, C., 2014. Spatiotemporal changes, faulting regimes, and source parameters of induced seismicity: A case study from the Geysers geothermal field. J. Geophys. Res. Solid Earth 119, 8378–8396. https://doi.org/10.1002/2014JB011385

Masayuki Kikuchi, and Hiroo Kanamori, 1982. Inversion of complex body waves. Bull. Seismol. Soc. Am. 72, 491–506.

McGuire, J.J., 2004. Estimating finite source properties of small earthquake ruptures. Bull. Seismol. Soc. Am. 94, 377–393. https://doi.org/10.1785/0120030091

McGuire, J.J., Zhao, L., Jordan, T.H., 2002. Predominance of unilateral rupture for a global catalog of large earthquake. Bull. Seismol. Soc. Am. 92, 3309–3317. https://doi.org/10.1785/0120010293

Okada, T., Matsuzawa, T., Umino, N., Yoshida, K., Hasegawa, A., Takahashi, H., Yamada, T., Kosuga, M., Takeda, T., Kato, A., Igarashi, T., Obara, K., Sakai, S., Saiga, A., Iidaka, T., Iwasaki, T., Hirata, N., Tsumura, N., Yamanaka, Y., Terakawa, T., Nakamichi, H., Okuda, T., Horikawa, S., Katao, H., Miura, T., Kubo, A., Matsushima, T., Goto, K., Miyamachi, H., 2016. Hypocenter migration and crustal seismic velocity distribution observed for the inland earthquake swarms induced by the 2011 Tohoku-Oki earthquake in NE Japan: Implications for crustal fluid distribution and crustal permeability, in: Crustal Permeability. https://doi.org/10.1002/9781119166573.ch24

Ross, Z.E., Rollins, C., Cochran, E.S., Hauksson, E., Avouac, J.P., Ben-Zion, Y., 2017. Aftershocks driven by afterslip and fluid pressure sweeping through a fault-fracture mesh. Geophys. Res. Lett. 44, 8260–8267. https://doi.org/10.1002/2017GL074634

Rutledge, J.T., Phillips, W.S., Mayerhofer, M.J., 2004. Faulting induced by forced fluid injection and fluid flow forced by faulting: An interpretation of hydraulic-fracture microseismicity, Carthage Cotton Valley gas field, Texas. Bull. Seismol. Soc. Am. 94, 1817–1830. https://doi.org/10.1785/012003257

Sato, T., Hirasawa, T., 1973. Body wave spectra from propagating shear cracks. J. Phys. Earth 21, 415–431. https://doi.org/10.4294/jpe1952.21.415

Seekins, L.C., Boatwright, J., 2010. Rupture directivity of moderate earthquakes in Northern California. Bull. Seismol. Soc. Am. 100, 1107–1119. https://doi.org/10.1785/0120090161

Shapiro, S.A., Huenges, E., Borm, G., 1997. Estimating the crust permeability from fluid-injection-induced seismic emission at the KTB site. Geophys. J. Int. 131. https://doi.org/10.1111/j.1365-246X.1997.tb01215.x

Shelly, D.R., Ellsworth, W.L., Hill, D.P., 2016. Fluid-faulting evolution in high definition: Connecting fault structure and frequency-magnitude variations during the 2014 Long Valley Caldera, California, earthquake swarm. J. Geophys. Res. Solid Earth 121, 1776–1795. https://doi.org/10.1002/2015JB012719

Tan, Y., Helmberger, D., 2010. Rupture directivity characteristics of the 2003 big bear sequence. Bull. Seismol. Soc. Am. 100, 1089–1106. https://doi.org/10.1785/0120090074

Terakawa, T., Hashimoto, C., Matsu'ura, M., 2013. Changes in seismic activity following the 2011 Tohoku-oki earthquake: Effects of pore fluid pressure. Earth Planet. Sci. Lett. 365, 17–24. https://doi.org/10.1016/j.epsl.2013.01.017

Tomic, J., Abercrombie, R.E., Do Nascimento, A.F., 2009. Source parameters and rupture velocity of small $M \leq 2.1$ reservoir induced earthquakes. Geophys. J. Int. 179, 1013–1023. https://doi.org/10.1111/j.1365-246X.2009.04233.x

Udias, A., Madariaga, R., Buforn, E., 2013. Source mechanisms of earthquakes: Theory and practice, Source Mechanisms of Earthquakes: Theory and Practice. https://doi.org/10.1017/CBO9781139628792

Urata, Y., Yoshida, K., Fukuyama, E., Kubo, H., 2017. 3-D dynamic rupture simulations of the 2016 Kumamoto, Japan, earthquake 4. Seismology. Earth, Planets Sp. 69, 150. https://doi.org/10.1186/s40623-017-0733-0

Venkataraman, A., Kanamori, H., 2004. Observational constraints on the fracture energy of subduction zone earthquakes. J. Geophys. Res. Solid Earth 109. https://doi.org/10.1029/2003JB002549

Waldhauser, F., Ellsworth, W.L., 2000. A Double-Difference Earthquake Location Algorithm : Method and Application to the Northern Hayward Fault, California

1353–1368.

Weertman, J., 1980. Unstable slippage across a fault that separates elastic media of different elastic constants. J. Geophys. Res. 85, 1455–1461. https://doi.org/10.1029/JB085iB03p01455

Wyss, M., 1973. Towards a Physical Understanding of the Earthquake Frequency Distribution. Geophys. J. R. Astron. Soc. 31, 341–359. https://doi.org/10.1111/j.1365-246X.1973.tb06506.x

Xue, L., Bürgmann, R., Shelly, D.R., Johnson, C.W., Taira, T., 2018. Kinematics of the 2015 San Ramon, California earthquake swarm: Implications for fault zone structure and driving mechanisms. Earth Planet. Sci. Lett. 489, 135–144. https://doi.org/10.1016/j.epsl.2018.02.018

Yamada, T., Mori, J.J., Ide, S., Kawakata, H., Iio, Y., Ogasawara, H., 2005. Radiation efficiency and apparent stress of small earthquakes in a South African gold mine. J. Geophys. Res. B Solid Earth 110, 1–18. https://doi.org/10.1029/2004JB003221

Ye, L., Lay, T., Kanamori, H., Rivera, L., 2016. Rupture characteristics of major and great (Mw≥ 7.0) megathrust earthquakes from 1990 to 2015: 1. Source parameter scaling relationships. J. Geophys. Res. Solid Earth 121, 826–844.

https://doi.org/10.1002/2015JB012426

Yoshida, K., Hasegawa, A., Okada, T., Iinuma, T., Ito, Y., Asano, Y., 2012. Stress before and after the 2011 great Tohoku-oki earthquake and induced earthquakes in inland areas of eastern Japan. Geophys. Res. Lett. 39. https://doi.org/10.1029/2011GL049729

Yoshida, K., Hasegawa, A., 2018a. Sendai-Okura earthquake swarm induced by the 2011 Tohoku-Oki earthquake in the stress shadow of NE Japan: Detailed fault structure and hypocenter migration. Tectonophysics 733, 132–147. https://doi.org/10.1016/j.tecto.2017.12.031

Yoshida, K., Hasegawa, A., 2018b. Hypocenter Migration and Seismicity Pattern Change in the Yamagata-Fukushima Border, NE Japan, Caused by Fluid Movement and Pore Pressure Variation. J. Geophys. Res. Solid Earth 123, 5000–5017. https://doi.org/10.1029/2018JB015468

Yoshida, K., Hasegawa, A., Okada, T., Iinuma, T., 2014. Changes in the stress field after the 2008 M7.2 Iwate-Miyagi Nairiku earthquake in northeastern Japan. J. Geophys. Res. Solid Earth 119, 9016–9030. https://doi.org/10.1002/2014JB011291

Yoshida, K., Hasegawa, A., Okada, T., 2015. Spatially heterogeneous stress field in the source area of the 2011 Mw 6.6 Fukushima-Hamadori earthquake, NE Japan, probably caused by static stress change. Geophys. J. Int. 201, 1062–1071. https://doi.org/10.1093/gji/ggv068

Yoshida, K., Hasegawa, A., Yoshida, T., 2016. Temporal variation of frictional strength in an earthquake swarm in NE Japan caused by fluid migration. J. Geophys. Res. Solid Earth 121, 5953–5965. https://doi.org/10.1002/2016JB013022

Yoshida, K., Saito, T., Urata, Y., Asano, Y., Hasegawa, A., 2017. Temporal Changes in Stress Drop, Frictional Strength, and Earthquake Size Distribution in the 2011 Yamagata-Fukushima, NE Japan, Earthquake Swarm, Caused by Fluid Migration. J. Geophys. Res. Solid Earth 122, 10,379-10,397. https://doi.org/10.1002/2017JB014334

Yoshida, K., Hasegawa, A., Yoshida, T., Matsuzawa, T., 2018. Heterogeneities in Stress and Strength in Tohoku and Its Relationship with Earthquake Sequences Triggered by the 2011 M9 Tohoku-Oki Earthquake. Pure Appl. Geophys. 1–21. https://doi.org/10.1007/s00024-018-2073-9

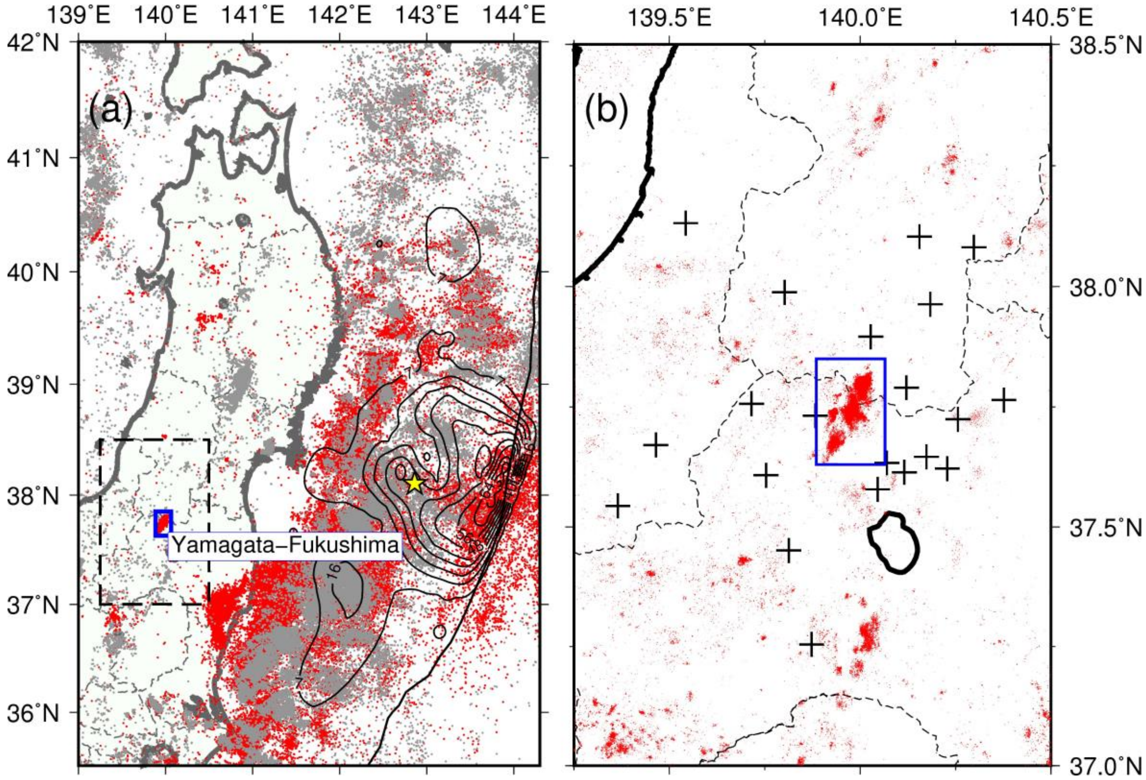

Figure 1. The earthquake swarm in the Yamagata-Fukushima border. The blue rectangle indicates the focal region of the swarm. Red and gray circles denote shallow earthquakes (z <40 km) before and after the 2011 Tohoku-Oki earthquake, respectively. (a) The distribution of hypocenters before and after the 2011 Tohoku-Oki earthquake. Gray circles denote shallow earthquakes before the 2011 Tohoku-Oki earthquake. The black contours show the coseismic slip distribution of the Tohoku-Oki earthquake determined by Iinuma et al. (2012). The dashed line rectangle indicates the range of (b). (b) The distribution of seismic stations around the source region of the Yamagata-Fukushima border swarm. Stations used in this study are shown by crosses.

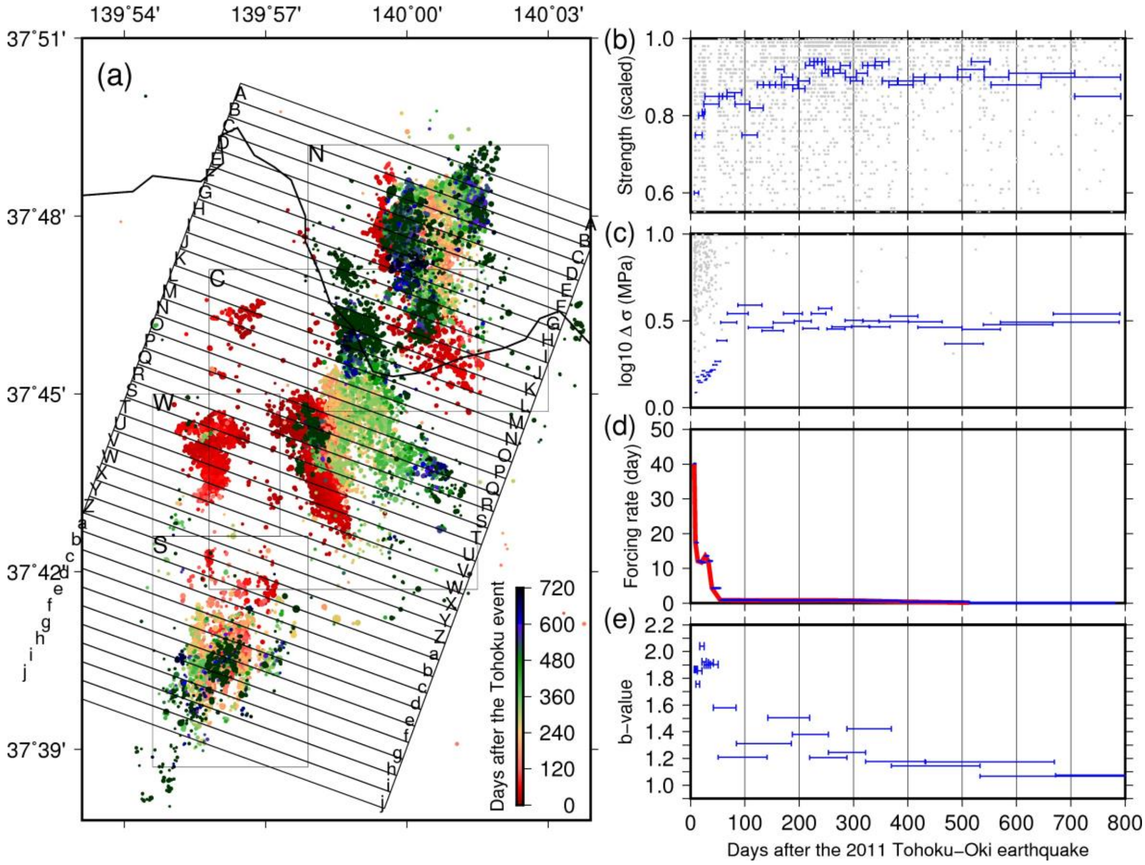

Figure 2. Temporal changes in the Yamagata-Fukushima border swarm. (a) Map view showing hypocenter migration. Dots show hypocenters of earthquakes. Time elapsed after the Tohoku-Oki earthquake is shown by the color scale. The thin line denotes the border line between Yamagata and Fukushima prefectures. (b)–(e) Temporal variations in (b) fault strength, (c) stress drop, (d) background seismicity rate, and (e) b-value. The horizontal lines show the time periods from which data were taken for computation of the corresponding values. Data for frictional strengths are from Yoshida et al. (2016), those for stress drops and b-values are from Yoshida et al. (2017), and those for background seismicity rate are from Yoshida & Hasegawa (2018b).

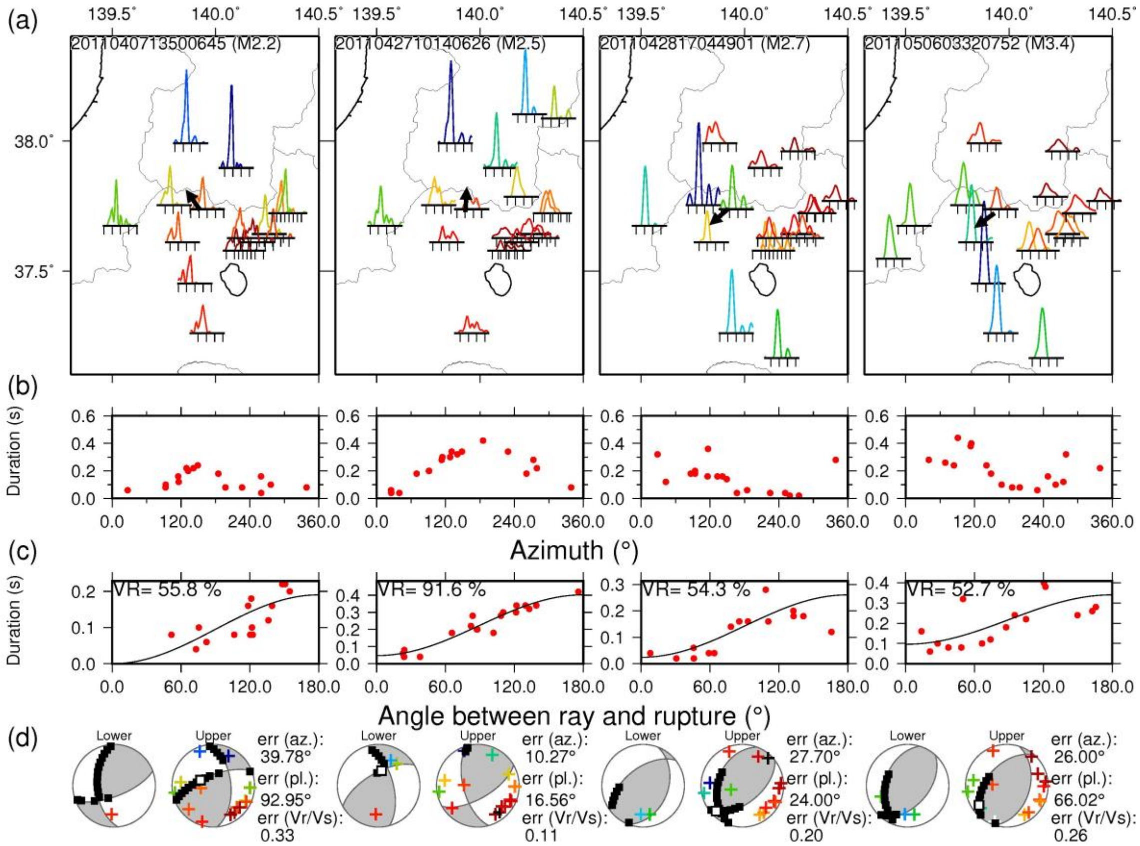

Figure 3. Four examples of the distribution of apparent moment rate functions. (a) Apparent moment rate functions plotted on the locations of seismic stations. Black arrows represent the azimuths of rupture directivity based on the unilateral rupture model. Tick marks denote 0.1 s intervals. (b) Relationships between azimuth of the seismic stations and the pulse widths of apparent moment rate functions. (c) Relationships between the angles between the ray and rupture, and the pulse widths of apparent moment rate functions. (d) Confidence regions of rupture propagation direction shown on the beach-balls. Crosses show the seismic stations. White squares shows the best-fit direction of rupture propagation. Black squares show results from 2,000 computations based on the bootstrap resampling. The results are shown in the left-beach ball (lower-hemisphere projection) when the ray or the rupture is downward. They are shown on the right-beach ball (upper-hemisphere projection) when the ray or the rupture is upward.

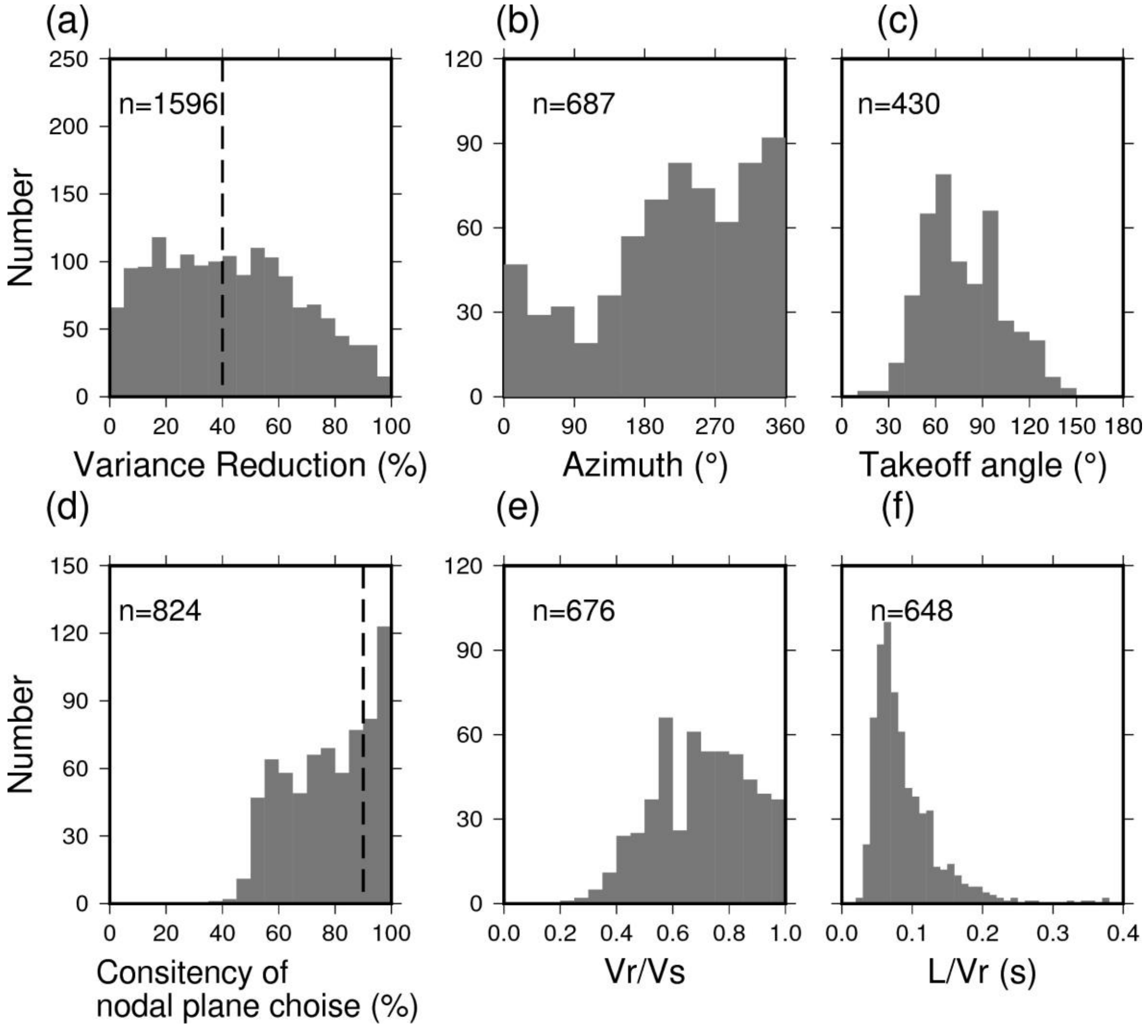

Figure 4. Results of applying the 1-D unilateral rupture model. They are shown by frequency distribution. (a) Variance reduction (VR), (b) azimuth of rupture propagation, (c) take-off angle of rupture propagation, (d) consistency of nodal plane choice, (e) Rupture velocity divided by S-wave velocity (Vr/Vs), (f) Rupture length divided by rupture speed (L/Vr). Azimuth, takeoff angle, Vr/Vs, and L/Vr are shown only when the variance reduction in (a) is higher than 40%.

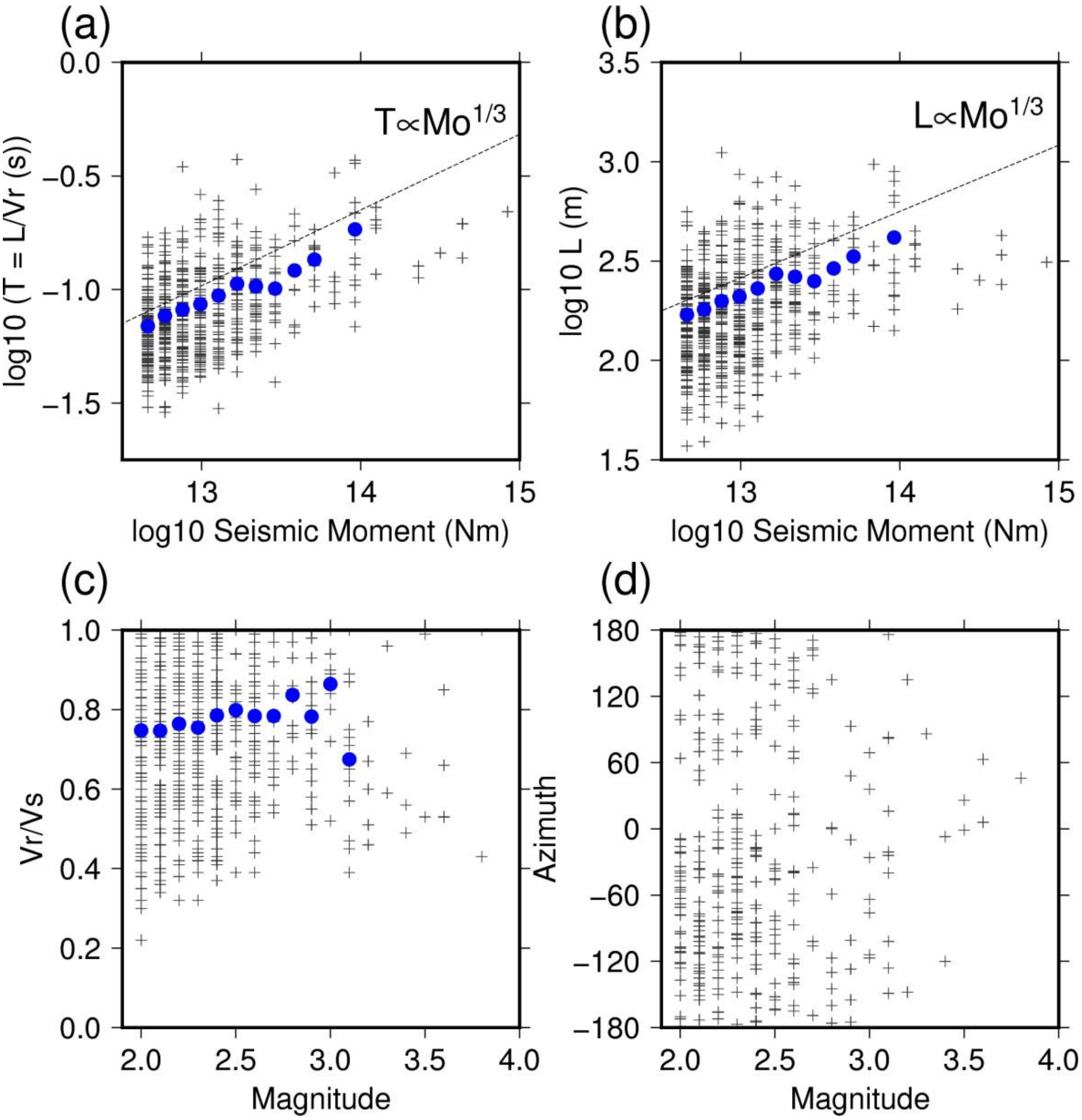

Figure 5. Comparisons of the results of applying the 1-D unilateral rupture model with the magnitude and the seismic moment. (a) seismic moment versus source duration, (b) seismic moment versus fault length, (c) magnitude versus VR/Vs, (d) magnitude versus azimuth. Crosses represent individual values. The blue circles show the mean values at each seismic moment and magnitude.

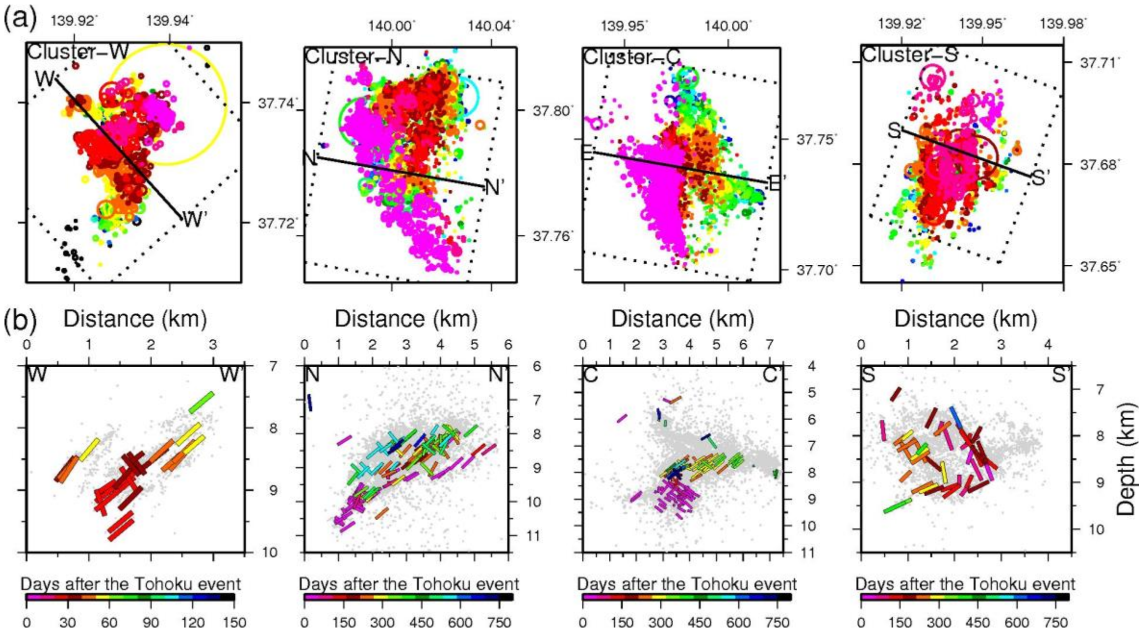

Figure 6. Hypocenter migrations and fault plane orientations in the four clusters. (a) Locations of hypocenters are shown in map view. The circle diameter corresponds to the circular fault size when the stress drop is 3 MPa. (b) Fault planes chosen based on the rupture directivity. Colors indicate the occurrence timing of earthquakes according to the color scale. Bar length corresponds to the angle of the maximum dip of the fault plane with the cross-section.

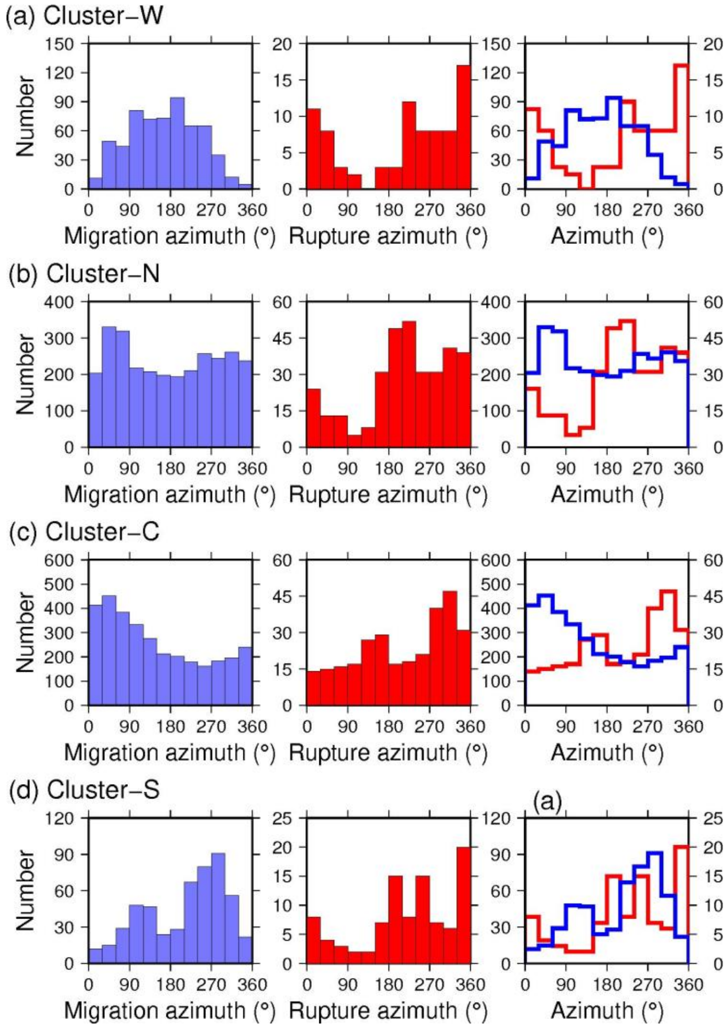

Figure 7. Comparison between the orientations of hypocenter migration and rupture propagation in the four clusters. Left: Frequency distribution of migration azimuth of hypocenters. Middle: Frequency distribution of azimuth of rupture propagation. Right: Comparison of frequency distributions of hypocenter migration and rupture.

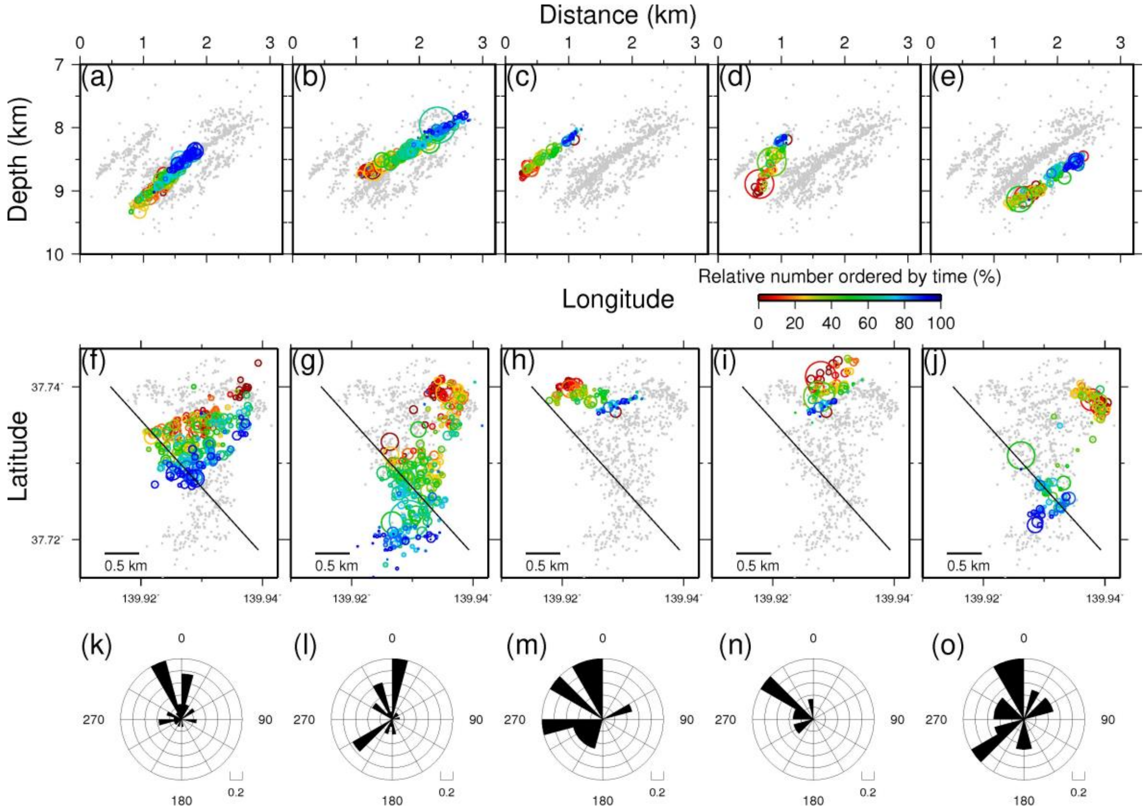

Figure 8. Orientations of rupture directivity and hypocenter migration on the five distinct planar structures in the western cluster. Five columns correspond to the five planes. (a)–(e): Hypocenters shown in the cross-sectional views along the lines in (f)–(j). (f)–(j): hypocenters shown in the map views. (k)–(o): rose diagrams showing the relative frequency of rupture propagation directions.

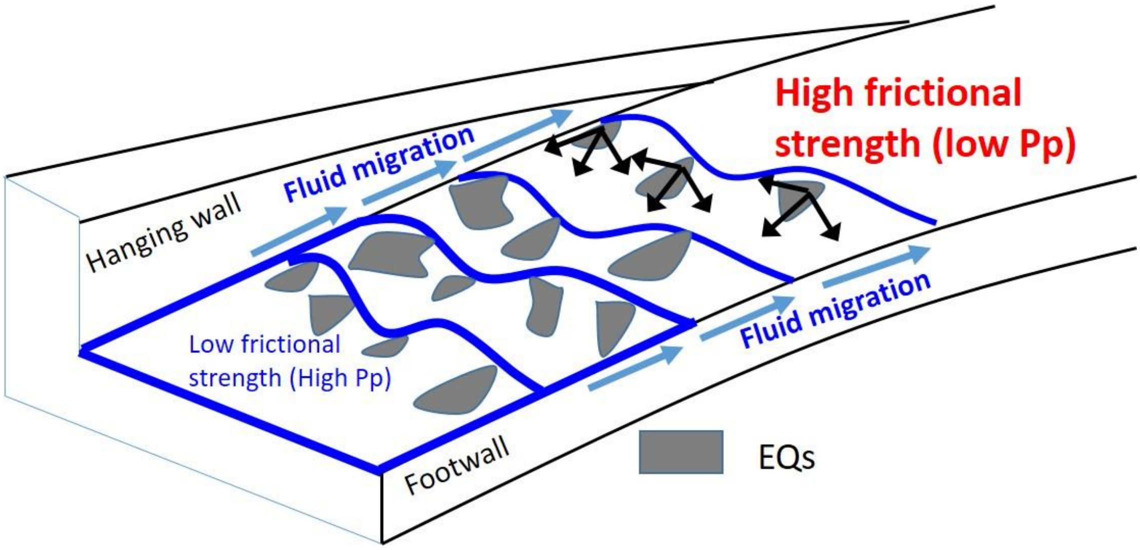

Figure 9. A schematic illustration explaining the relationship of directions between the rupture propagation and the hypocenter migration. Pore-pressure migrates along the plane together with hypocenters. Lower pore pressure and hence higher fault strength tend to hinder the propagation of rupture outward of the pore-pressure front (shallower development) while higher pore pressure tends to allow rupture to propagate inward.

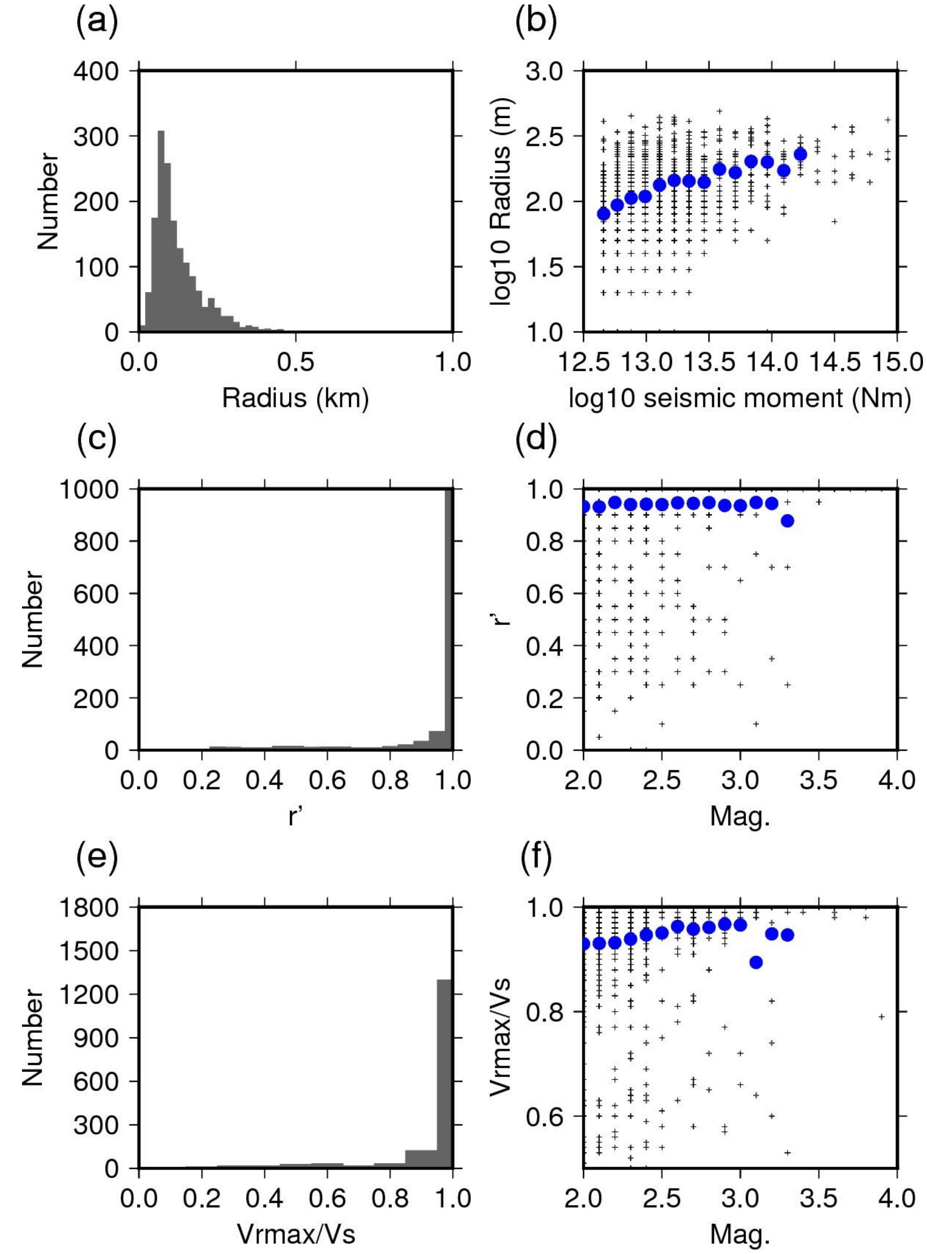

Figure 10. Results of applying the asymmetrical circular crack model. (a) Frequency distributions of fault radii and (b) their relationship with magnitude. (c) Frequency distributions of relative distance of the initiation points from the center to the fault radius, and (d) their relationship with magnitude. (e) Frequency distributions of ratios between the maximum rupture velocity and the S-wave velocity, and (f) their relationship with magnitude. The blue circles represent the mean value at each magnitude.

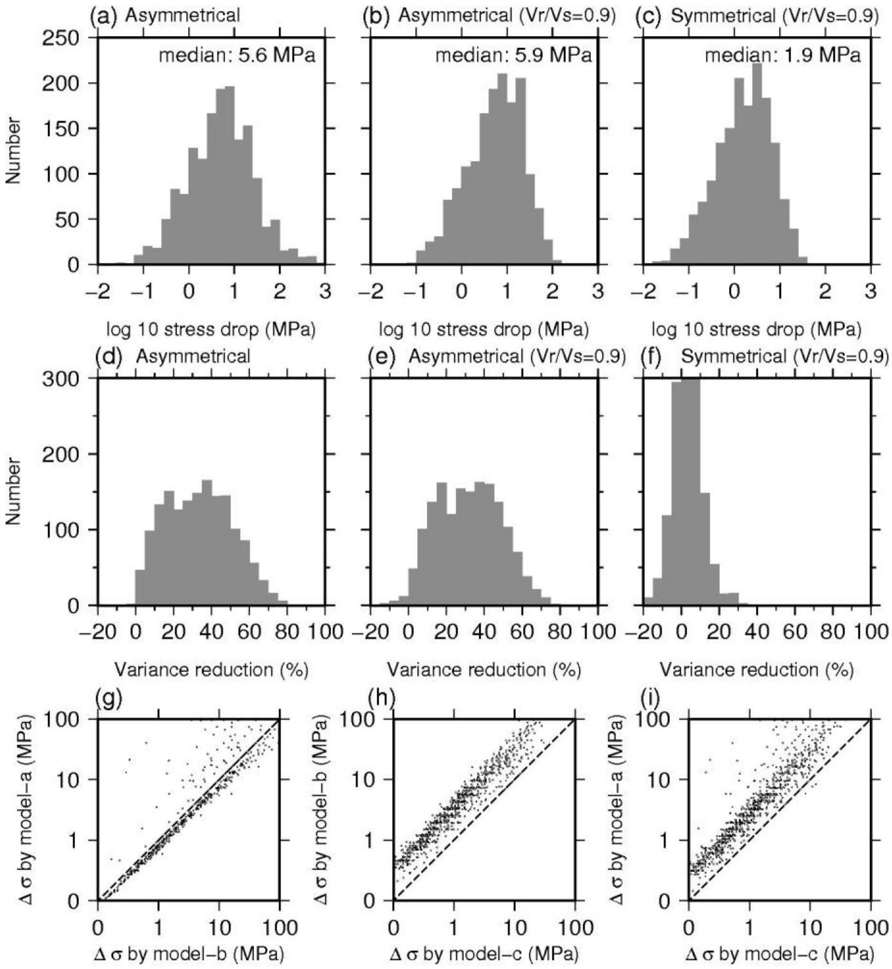

Figure 11. Results of stress drop. (a), (b), and (c) show frequency distribution of stress drops estimated based on the asymmetrical circular crack model, those based on the asymmetrical circular crack model with constant Vr/Vs=0.9, and those based on the symmetrical circular crack model with constant Vr/Vs=0.9, respectively. (d), (e) and (f) show frequency distribution of variance reduction of the corresponding models. (g) Comparison between stress drops based on the asymmetrical model (a) and those based on the asymmetrical model (b) with constant Vr/Vs=0.9 of same events. (h) Comparison between stress drops based on the asymmetrical model (b) and those based on the symmetrical model (c) of same events. (i) Comparison between stress drops based on the asymmetrical model (a) and those based on the symmetrical model (c) of same events.

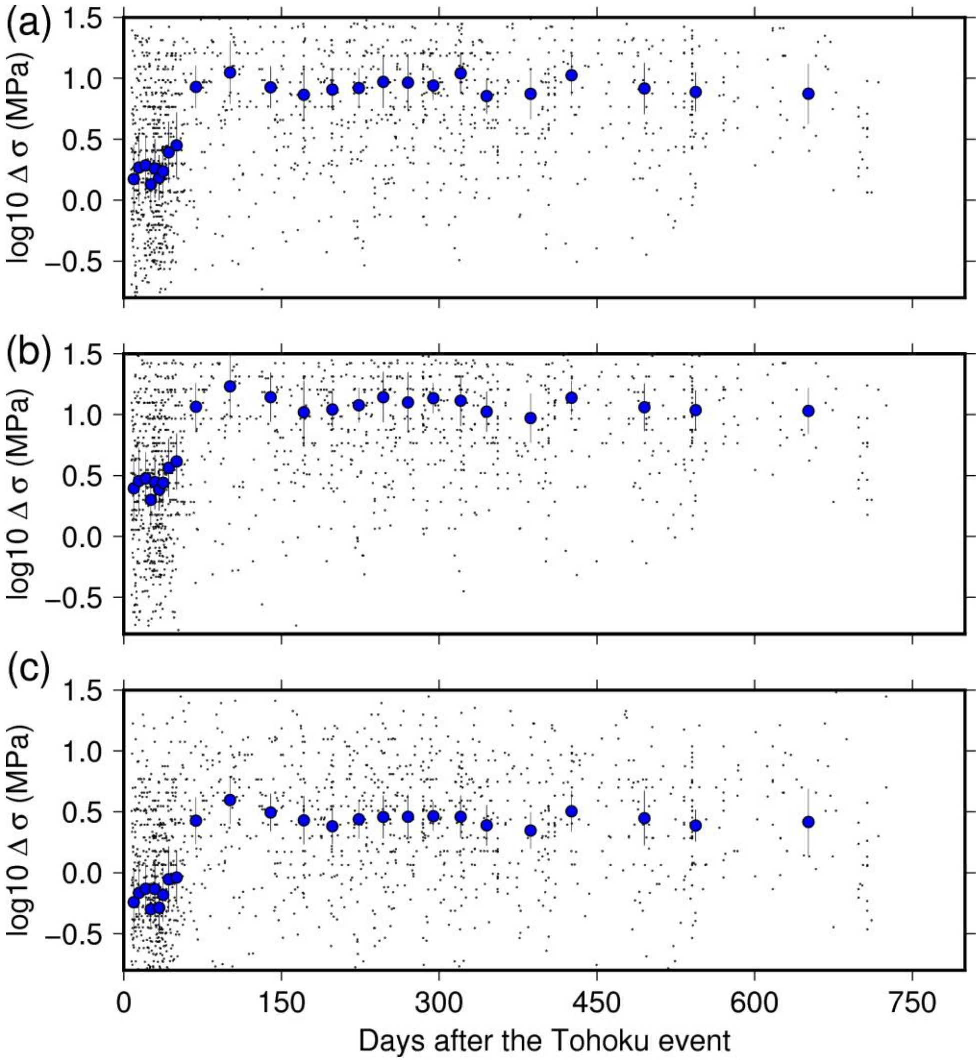

Figure 12. Temporal changes in stress drop. Gray dots represent the individual results. Blue circles and vertical values are the median values and the 95 % confidence interval, respectively. (a) stress drop estimated based on the asymmetrical circular crack model. (b) stress drop estimated based on the asymmetrical circular crack model with constant Vr/Vs=0.9. (c) stress drop estimated based on the symmetrical circular crack model with constant Vr/Vs = 0.9.

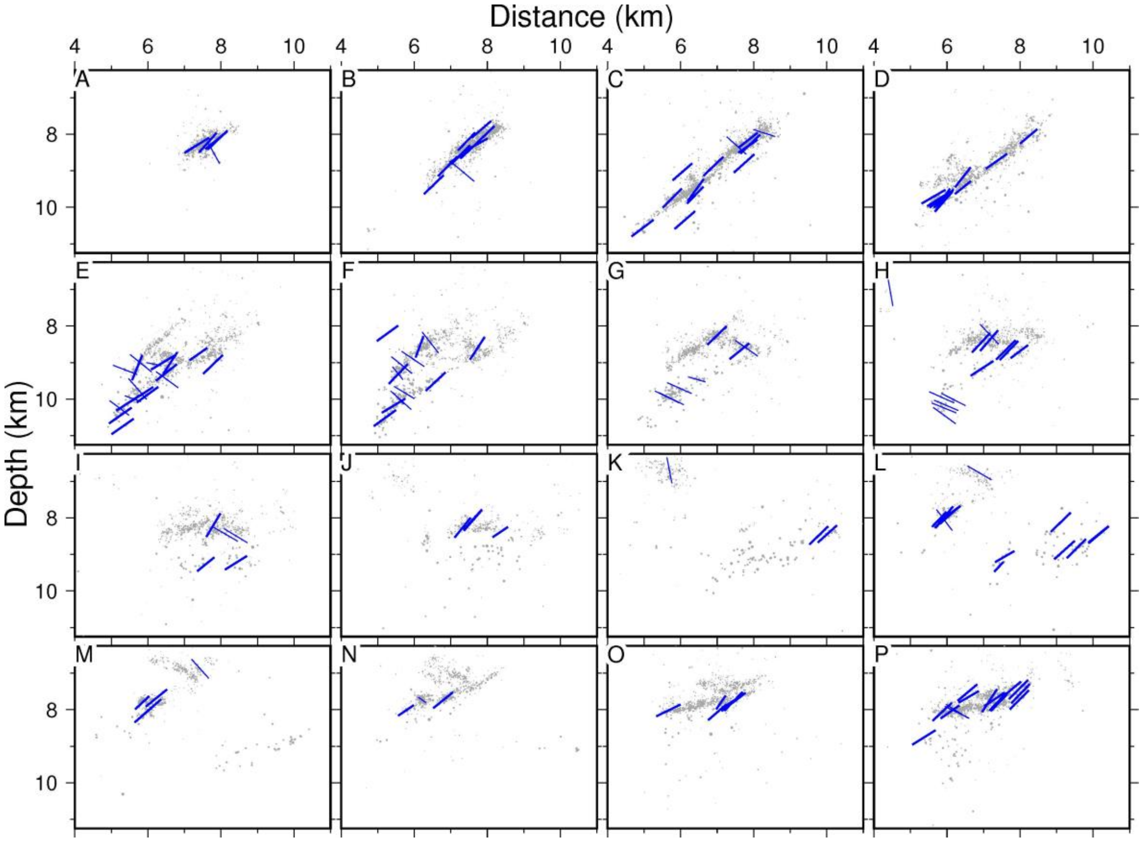

Figure 13. Orientations of fault planes and hypocenter distribution in the northern and southern cluster. Blue bars indicate the orientation of fault planes. Bar length corresponds to the angle of the maximum dip of fault plane with the cross-section.

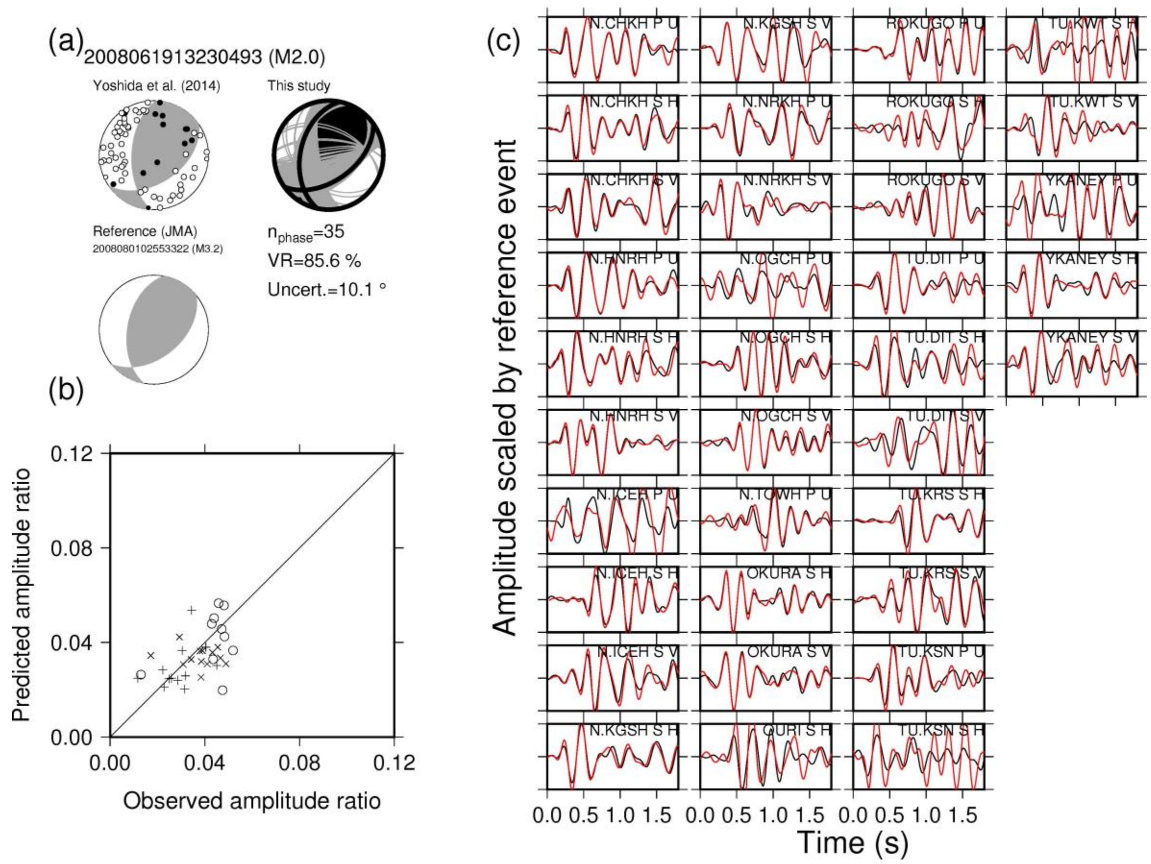

Figure A1. An example of applying the focal mechanism determination method used in this study. (a) Focal mechanisms determined by Yoshida et al. (2014) (left) and in this study (right) are shown beach-balls. Black and white circles in the left beach-ball represent first-motion polarity data (up and down, respectively). The gray curves in the right figure indicate 1,000 solutions based on the bootstrap resampling. The beach-ball on the lower left indicates the reference focal mechanism listed in the JMA catalog. (b) Comparison between observed and theoretical amplitude ratio data. (c) Examples of waveform data. Red waveforms represent the waveforms of the reference event, and black represents waveforms of the target event divided by the predicted amplitude ratio of the two earthquakes.

Figure Captions

Figure 1. The earthquake swarm in the Yamagata-Fukushima border. The blue rectangle indicates the focal region of the swarm. Red and gray circles denote shallow earthquakes (z <40 km) before and after the 2011 Tohoku-Oki earthquake, respectively. (a) The distribution of hypocenters before and after the 2011 Tohoku-Oki earthquake. Gray circles denote shallow earthquakes before the 2011 Tohoku-Oki earthquake. The black contours show the coseismic slip distribution of the Tohoku-Oki earthquake determined by Iinuma et al. (2012). The dashed line rectangle indicates the range of (b). (b) The distribution of seismic stations around the source region of the Yamagata-Fukushima border swarm. Stations used in this study are shown by crosses.

Figure 2. Temporal changes in the Yamagata-Fukushima border swarm. (a) Map view showing hypocenter migration. Dots show hypocenters of earthquakes. Time elapsed after the Tohoku-Oki earthquake is shown by the color scale. The thin line denotes the border line between Yamagata and Fukushima prefectures. (b)–(e) Temporal variations in (b) frictional strength, (c) stress

drop, (d) background seismicity rate, and (e) b-value. The horizontal lines show the time periods from which data were taken for computation of the corresponding values. Data for frictional strengths are from Yoshida et al. (2016), those for stress drops and b-values are from Yoshida et al. (2017), and those for background seismicity rate are from Yoshida & Hasegawa (2018b).

Figure 3. Four examples of the distribution of apparent moment rate functions. (a) Apparent moment rate functions plotted on the locations of seismic stations. Black arrows represent the azimuths of rupture directivity based on the unilateral rupture model. Tick marks denote 0.1 s intervals. (b) Relationships between azimuth of the seismic stations and the pulse widths of apparent moment rate functions. (c) Relationships between the angles between the ray and rupture, and the pulse widths of apparent moment rate functions. (d) Confidence regions of rupture propagation direction shown on the beach-balls. Crosses show the seismic stations. White squares show the best-fit direction of rupture propagation. Black squares show results from 2,000 computations based on the bootstrap resampling. The results are

shown in the left-beach ball (lower-hemisphere projection) when the ray or the rupture is downward. They are shown on the right-beach ball (upper-hemisphere projection) when the ray or the rupture is upward.

Figure 4. Results of applying the 1-D unilateral rupture model. They are shown by frequency distribution. (a) Variance reduction (VR), (b) azimuth of rupture propagation, (c) take-off angle of rupture propagation, (d) consistency of nodal plane choice, (e) Rupture velocity divided by S-wave velocity (Vr/Vs), (f) Rupture length divided by rupture speed (L/Vr). Azimuth, takeoff angle, Vr/Vs, and L/Vr are shown only when the variance reduction in (a) is higher than 40%.

Figure 5. Comparisons of the results of applying the 1-D unilateral rupture model with the magnitude and the seismic moment. (a) seismic moment versus source duration, (b) seismic moment versus fault length, (c) magnitude versus VR/Vs, (d) magnitude versus azimuth. Crosses represent individual values. The blue circles show the mean values at each seismic moment and magnitude.

Figure 6. Hypocenter migrations and fault plane orientations in the four clusters. (a) Locations of hypocenters are shown in map view. The circle diameter corresponds to the circular fault size when the stress drop is 3 MPa. (b) Fault planes chosen based on the rupture directivity. Colors indicate the occurrence timing of earthquakes according to the color scale. Bar length corresponds to the angle of the maximum dip of the fault plane with the cross-section.

Figure 7. Comparison between the orientations of hypocenter migration and rupture propagation in the four clusters. Left: Frequency distribution of migration azimuth of hypocenters. Middle: Frequency distribution of azimuth of rupture propagation. Right: Comparison of frequency distributions of hypocenter migration and rupture.

Figure 8. Orientations of rupture directivity and hypocenter migration on the five distinct planar structures in the western cluster. Five columns correspond to the five planes. (a)–(e): Hypocenters shown in the cross-sectional views

along the lines in (f)–(j). (f)–(j): hypocenters shown in the map views. (k)–(o): rose diagrams showing the relative frequency of rupture propagation directions.

Figure 9. A schematic illustration explaining the relationship of directions between the rupture propagation and the hypocenter migration. Pore-pressure migrates along the plane together with hypocenters. Lower pore pressure and hence higher fault strength tend to hinder the propagation of rupture outward of the pore-pressure front (shallower development) while higher pore pressure tends to allow rupture to propagate inward.

Figure 10. Results of applying the asymmetrical circular crack model. (a) Frequency distributions of fault radii and (b) their relationship with magnitude. (c) Frequency distributions of relative distance of the initiation points from the center to the fault radius, and (d) their relationship with magnitude. (e) Frequency distributions of ratios between the maximum rupture velocity and the S-wave velocity, and (f) their relationship with magnitude. The blue circles represent the mean value at each magnitude.

Figure 11. Results of stress drop. (a), (b), and (c) show frequency distribution of stress drops estimated based on the asymmetrical circular crack model, those based on the asymmetrical circular crack model with constant Vr/Vs=0.9, and those based on the symmetrical circular crack model with constant Vr/Vs=0.9, respectively. (d), (e) and (f) show frequency distribution of variance reduction of the corresponding models. (g) Comparison between stress drops based on the asymmetrical model (a) and those based on the asymmetrical model (b) with constant Vr/Vs=0.9 of same events. (h) Comparison between stress drops based on the asymmetrical model (b) and those based on the symmetrical model (c) of same events. (i) Comparison between stress drops based on the asymmetrical model (a) and those based on the symmetrical model (c) of same events.

Figure 12. Temporal changes in stress drop. Gray dots represent the individual results. Blue circles and vertical values are the median values and the 95 % confidence interval, respectively. (a) stress drop estimated based on the asymmetrical circular crack model. (b) stress drop estimated based on the

asymmetrical circular crack model with constant Vr/Vs=0.9. (c) stress drop estimated based on the symmetrical circular crack model with constant Vr/Vs = 0.9.

Figure 13. Orientations of fault planes and hypocenter distribution in the northern and southern cluster. Blue bars indicate the orientation of fault planes. Bar length corresponds to the angle of the maximum dip of fault plane with the cross-section.

Figure A1. An example of applying the focal mechanism determination method used in this study. (a) Focal mechanisms determined by Yoshida et al. (2014) (left) and in this study (right) are shown beach-balls. Black and white circles in the left beach-ball represent first-motion polarity data (up and down, respectively). The gray curves in the right figure indicate 1,000 solutions based on the bootstrap resampling. The beach-ball on the lower left indicates the reference focal mechanism listed in the JMA catalog. (b) Comparison between observed and theoretical amplitude ratio data. (c) Examples of waveform data. Red waveforms represent the waveforms of the reference event, and black represents waveforms of the target event divided by the predicted amplitude ratio of the two earthquakes.

Supplementary Figures

Figure S1. Distribution of the hypocenters relocated in this study. Blue dots represent the hypocenters. The 36 figures show across-fault vertical cross-sections along the lines shown in Fig. 2 (a). Their colors show the occurrence time in accordance with Fig. 2(a).

Figure S2. Distribution of focal mechanisms shown in map view. Focal mechanisms are shown by “beach balls”. Red, green, and blue “beach balls” denote thrust, strike-slip, and normal fault types of focal mechanisms, respectively, whose plunges of T, P, and B axes were greater than 45°.

Figure S3. Distribution of focal mechanisms shown in cross-sectional view. Locations of cross-sections are shown in Fig. S2. Red, green, and blue “beach balls” denote thrust, strike-slip, and normal fault types of focal mechanisms, respectively, whose plunges of T, P, and B axes were greater than 45°.

Figure S4. Comparison of VR with ΔAIC. (a) ΔAIC against VR for each event. (b) Percentage of positive ΔAIC above corresponding VR.

Figure S5. Temporal changes in Vr/Vs. Gray dots represent the individual results. Median stress drops were computed in 25 time-windows having the same number of results. Blue circles and vertical values are the median values and the 95 % confidence interval, respectively.